

Berry curvature dipole senses topological transition in a moiré superlattice

Subhajit Sinha^{1†*}, Pratap Chandra Adak^{1†}, Atasi Chakraborty², Kamal Das², Koyendrila Debnath³, L. D. Varma Sangani¹, Kenji Watanabe⁴, Takashi Taniguchi⁵, Umesh V. Waghmare³, Amit Agarwal^{2*}, and Mandar M. Deshmukh^{1*}

¹*Department of Condensed Matter Physics and Materials Science, Tata Institute of Fundamental Research, Homi Bhabha Road, Mumbai 400005, India.*

²*Department of Physics, Indian Institute of Technology, Kanpur 208016, India.*

³*Theoretical Sciences Unit, Jawaharlal Nehru Centre for Advanced Scientific Research, Bangalore 560064, India.*

⁴*Research Center for Functional Materials, National Institute for Materials Science, 1-1 Namiki, Tsukuba 305-0044, Japan.*

⁵*International Center for Materials Nanoarchitectonics, National Institute for Materials Science, 1-1 Namiki, Tsukuba 305-0044, Japan.*

[†]These two authors contributed equally to this work

*sinhasubhajit25@gmail.com, amitag@iitk.ac.in, deshmukh@tifr.res.in

Topological aspects of electron wavefunction play a crucial role in determining the physical properties of materials. Berry curvature and Chern number are used to define the topological structure of electronic bands. While Berry curvature and its effects in materials have been studied [1, 2], detecting changes in the topological invariant, Chern number, is challenging. In this regard, twisted double bilayer graphene (TDBG) [3–7] has emerged as a promising platform to gain electrical control over the Berry curvature hotspots [8] and the valley Chern numbers of its flat bands [9, 10]. In addition, strain induced breaking of the three-fold rotation (C_3) symmetry in TDBG, leads to a non-zero first moment of Berry curvature called the Berry curvature dipole (BCD), which can be sensed using nonlinear Hall (NLH) effect [11]. We reveal, using TDBG, that the BCD detects topological transitions in the bands and changes

its sign. In TDBG, the perpendicular electric field tunes the valley Chern number and the BCD simultaneously allowing us a tunable system to probe the physics of topological transitions. Furthermore, we find hysteresis of longitudinal and NLH responses with electric field that can be attributed to switching of electric polarization in moiré systems. Such a hysteretic response holds promise for next-generation Berry curvature-based memory devices. Probing topological transitions, as we show, can be emulated in other 3D topological systems.

Exploring materials with new topological phases and probing their symmetries has been at the forefront of modern research. Topology is often characterized by Berry curvature that manifests as quantum Hall effect [1] or as anomalous Hall effect in magnetic materials [1, 2]. While these effects have led to many breakthroughs in physics, these linear responses vanish in systems that preserve time-reversal symmetry. However,

even in time-reversal symmetry protected systems, broken inversion symmetry can lead to the first moment of Berry curvature, namely Berry curvature dipole (BCD), when further spatial symmetries are reduced [11]. In presence of an ac current (of frequency ω) in such system, the BCD can drive a second-order electrical response, namely the nonlinear Hall (NLH) voltage with zero (DC) and second-harmonic (2ω) frequency. Aligned with the recent interest in various nonlinear phenomena such as nonlinear optics, there is a rapidly growing interest to look for quantum materials that host the NLH effect [12, 13].

The topological phase of quantum materials can be characterized by the band-specific topological invariant Chern number. Often systems undergo transition between topological phases and these transitions are hard to detect, unlike phase transitions of order parameter. Recent proposals suggest that topological transitions are accompanied by simultaneous changes in BCD [14, 15]. Moiré systems are known to be natural candidates to host topological bands [16]. While the NLH effect has been observed for transition metal dichalcogenides (TMDCs) [17–21] and corrugated bilayer graphene [22], the experimental study in two-dimensional moiré systems is limited [23]. Furthermore, topological transitions along with BCD have not been experimentally observed thus far.

Recently, the observation of several novel phenomena in moiré systems such as magic-angle twisted bilayer graphene has attracted attention [24–29]. Flat bands in twistrionic systems give rise to various electron correlation phenomena such as Mott insulators and superconductivity [24–27]. In particular, the observation of anomalous Hall effect and orbital ferromagnetism point to the rich topology of these twisted systems [28, 29]. Flat bands of moiré systems are also susceptible to symmetry breaking by strain [30]. Together with the fact that spatial symmetry breaking can lead to nonzero BCD [30–32], bands in 2D moiré systems offer an interesting platform to electrically tune topology and detect it via the NLH effect.

In this work, we use twisted double bilayer graphene (TDBG), in which two copies of bilayer

graphene are stacked together with a small twist angle $\sim 1.1^\circ$, as a candidate system to study topological transitions using the NLH effect. While the flat bands in TDBG host correlation induced physics as in twisted bilayer graphene, TDBG is additionally equipped with electric field tunability [3–7, 33]. The perpendicular electric field, apart from modulating the band structure, can also change the valley Chern number of a flat band [10]. Additionally, almost touching flat bands with small tunable energy gaps of few meV in TDBG gives rise to large Berry curvature in this system [8, 16, 34]. We use electric field tunability to demonstrate that TDBG hosts substantially large BCD due to strain. The BCD changes sign abruptly and this can be attributed to a topological transition, a change in valley Chern number, with the electric field. Additionally, hysteresis in both longitudinal resistance and NLH signal as a function of the electric field suggests switching between metastable states.

In TDBG, broken inversion symmetry allows nonzero Berry curvature (Ω). Additionally, imaging of small-angle twisted moiré devices reveals strain that breaks three-fold rotational (C_3) symmetry [23, 35, 36]. Such reduced symmetry makes the Berry curvature distribution non-symmetric and anisotropic over the moiré Brillouin zone (mBZ), leading to nonzero BCD (Λ_α) given by,

$$\Lambda_\alpha = \sum_n \int_{\text{mBZ}} \frac{d\mathbf{k}}{(2\pi)^2} \Omega_z^n \frac{\partial \epsilon_{\mathbf{k}}^n}{\hbar \partial k_\alpha} \frac{\partial f(\epsilon_{\mathbf{k}}^n)}{\partial \epsilon_{\mathbf{k}}^n}. \quad (1)$$

Here α stands for the spatial index (x, y), $\epsilon_{\mathbf{k}}^n$ is the energy of the n^{th} band and $f(\epsilon_{\mathbf{k}}^n)$ is the Fermi-Dirac function. In Eq. (1), a sum over all the bands crossing the Fermi energy is implied. To calculate the BCD in TDBG, we consider distorted hexagonal moiré Brillouin zone with the C_3 symmetry broken by strain as shown in the schematic of Fig. 1a. The effect of C_3 symmetry breaking is reflected in the Berry curvature plots of Fig. 1b, c. Figure 1d shows the band structure for TDBG with a twist angle of 1.10° under 0.1% strain with Ω_z of the flat bands indicated by the color. Together, nonzero Berry

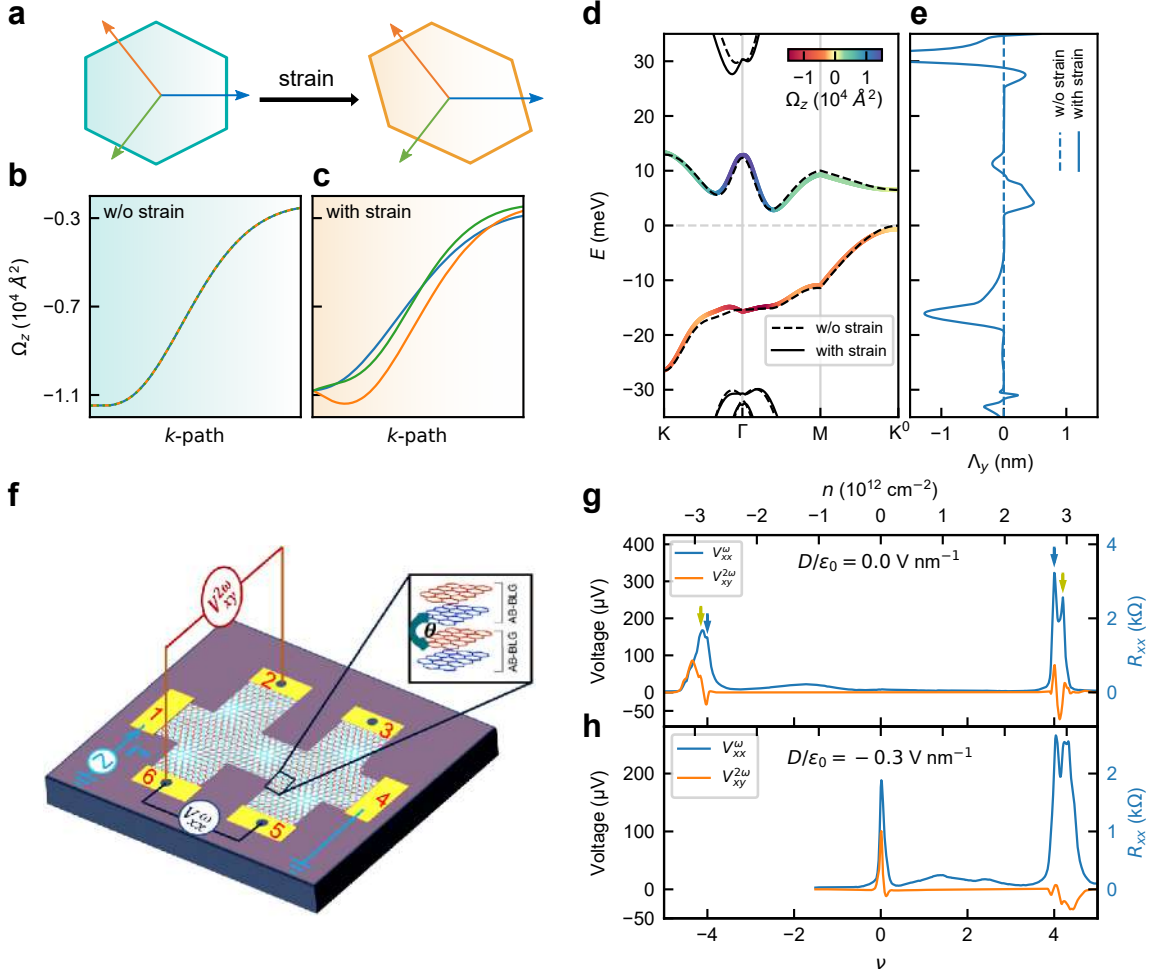


Fig. 1. Strain-mediated nonlinear Hall (NLH) effect in twisted double bilayer graphene (TDBG). **a**, Schematic shows the distortion of the hexagonal moiré Brillouin zone due to strain, that breaks the C_3 symmetry. **b**, **c**, The Berry curvature (Ω_z) of the valence band without strain (**b**) and with strain (**c**) along three paths arranged in 120° angle as shown in **a**. **d**, The band structure of 1.10° TDBG device with (solid lines) and without (dashed lines) 0.1% strain for an inter-layer potential of 11 meV, which opens up a gap between the low-energy flat bands along with finite moiré gaps. The energy is measured from the Fermi energy for zero doping. The overlaid color indicates the Berry curvature of the flat bands. **e**, The corresponding variation of the y -component of the Berry curvature dipole (Λ_y) for the 0.1% strained (solid line) and unstrained (dashed line) cases at 2 K. In the absence of strain there is no Berry curvature dipole due to the presence of the C_3 symmetry. **f**, Schematic of the NLH voltage measurement scheme without the encapsulating hBNs and top metal gate for clarity. When a current (I) with frequency ω is sent from 1-4, the voltage drop between 6-5 at frequency ω gives the longitudinal voltage V_{xx}^ω and the voltage drop between 2-6 at frequency 2ω gives the NLH voltage $V_{xy}^{2\omega}$. The schematic of TDBG in the inset indicates the two Bernal stacked AB bilayer graphenes, with an intermediate twist angle of $\theta = 1.10^\circ$. **g**, **h**, NLH voltage ($V_{xy}^{2\omega}$) (orange) and longitudinal voltage (V_{xx}^ω) (blue) vs. filling factor (ν) at $D/\epsilon_0 = 0$ V nm $^{-1}$ (**g**) and $D/\epsilon_0 = -0.3$ V nm $^{-1}$ (**h**). The data is taken at 1.5 K with a current of 100 nA. The right axes indicate the corresponding longitudinal resistance, R_{xx} . The two peaks in V_{xx}^ω at $\nu = \pm 4$, marked by blue and green arrows in **g**, indicate moiré peaks due to an angle inhomogeneity of $\sim 0.03^\circ$, a signature of strain. The data in **h** is truncated towards negative ν due to restrictions in gate voltage that can be applied without causing a dielectric breakdown of the hBN.

curvature and broken C_3 symmetry generate a nonzero BCD, as shown in Fig. 1e (see Methods and Supplementary Information section I-III for calculations).

We fabricate multiple TDBG devices to measure NLH voltage, which probes the BCD [11, 18]. The dual-gate geometry allows independent control of the charge density (n) and the perpendicular electric displacement field (D) (see Methods). Figure 1f shows our measurement schematic to probe NLH effect. We send a current with low-frequency ω and measure the longitudinal voltage (V_{xx}^ω) and the second-harmonic NLH voltage ($V_{xy}^{2\omega}$) at frequencies ω and 2ω , respectively. In Fig. 1g, we show V_{xx}^ω and $V_{xy}^{2\omega}$ as a function of moiré filling factor (ν) at zero displacement field for a TDBG device with twist angle 1.10° . Here $\nu = 4n/n_s$ with n_s representing the number of carriers to fill one moiré band and factor 4 due to four-fold degeneracy of spin and valley. Peaks in V_{xx}^ω at $\nu = \pm 4$ correspond to the two moiré gaps. The substructures in the peaks of V_{xx}^ω (indicated by arrows) result from slightly different twist angles, indicating an angle inhomogeneity of $\sim 0.03^\circ$ – a signature of strain [36] that causes BCD in our system. In Fig. 1h, we plot V_{xx}^ω and $V_{xy}^{2\omega}$ for a non-zero perpendicular displacement field that creates a gap at $\nu = 0$ (charge neutrality point, CNP). We find NLH voltage $V_{xy}^{2\omega}$ is high in the vicinity of band edge around the moiré gaps at $\nu = \pm 4$ and the CNP gap in our strained TDBG devices.

We now study the evolution of V_{xx}^ω and the corresponding resistance (R_{xx}) in the experimentally accessible parameter space of ν and D in Fig. 2a. Schematics adjacent to Fig. 2a show change in the underlying band structure with D (see Supplementary Information section III for calculated band structure). A finite displacement field opens up a gap at CNP between the conduction and the valence flat bands. These flat bands are separated from the remote moiré bands by two moiré gaps, which close at larger values of D . Apart from the peaks in V_{xx}^ω corresponding to the CNP gap at $\nu = 0$ and the moiré gaps at $\nu = \pm 4$, we observe other features like the cross towards the hole side ($-4 < \nu < 0$) and the halo around $D/\epsilon_0 = \pm 0.3 \text{ V nm}^{-1}$ towards

the electron side ($0 < \nu < 4$). These characteristic features of TDBG within partial fillings of the flat bands are likely to be connected to structures in the density of states [33].

Figure 2b shows the evolution of the NLH voltage $V_{xy}^{2\omega}$ in the same parameter space of ν and D . In Fig. 2c, we have plotted few line slices of $V_{xy}^{2\omega}$ around $\nu = 0$ for different D . We find that $V_{xy}^{2\omega}$ peaks near the gaps at $\nu = 0$ (CNP gap) and $\nu = \pm 4$ (moiré gaps). The coincidence of the NLH voltage with the TDBG bandgaps reveals that the Berry curvature hotspots, and hence the BCD, reside predominantly in the vicinity of the band edges. We explore this behavior further in Fig. 3.

$V_{xy}^{2\omega}$ that we measure should scale quadratically with the in-plane ac electric field of frequency ω . To verify the quadratic scaling, we plot $V_{xy}^{2\omega}$ against the square of simultaneously measured V_{xx}^ω for two different (ν, D) biasing points in Fig. 2d. The linear behavior of $V_{xy}^{2\omega}$ with the square of V_{xx}^ω confirms the quadratic scaling near both the CNP gap and the moiré gaps. Additionally, $V_{xy}^{2\omega}$ switches sign when we reverse the Hall voltage probes and the direction of current simultaneously as depicted in Fig. 2e. These observations clearly demonstrate the second-order nature of the measured NLH voltage, $V_{xy}^{2\omega}$.

Having established $V_{xy}^{2\omega}$ as NLH voltage, we now use D as a parameter to study scaling between normalized NLH voltage $V_{xy}^{2\omega}/(V_{xx}^\omega)^2$ and square of longitudinal conductivity (σ_{xx}^2). Such scaling can be used to quantify BCD, as discussed later. In Fig. 3a, we plot $V_{xy}^{2\omega}/(V_{xx}^\omega)^2$ (left axis) and σ_{xx}^2 (right axis) as a function of D for $\nu = 0.125$ (indicated by the green vertical line in inset of Fig. 3a). The metallic behavior at $\nu = 0.125$ ensures that the Fermi energy is near the band edge (see Extended Data Fig. 3a for the temperature (T) dependence of R_{xx}). Both $V_{xy}^{2\omega}/(V_{xx}^\omega)^2$ and σ_{xx}^2 show different trends in two different regimes of the displacement field separated at $D/\epsilon_0 = -0.23 \text{ V nm}^{-1}$. Interestingly, the two regimes are characterized by different band structures – in regime-I, the flat bands are gapped and are isolated from the remote moiré bands, while in regime-II the valence flat band

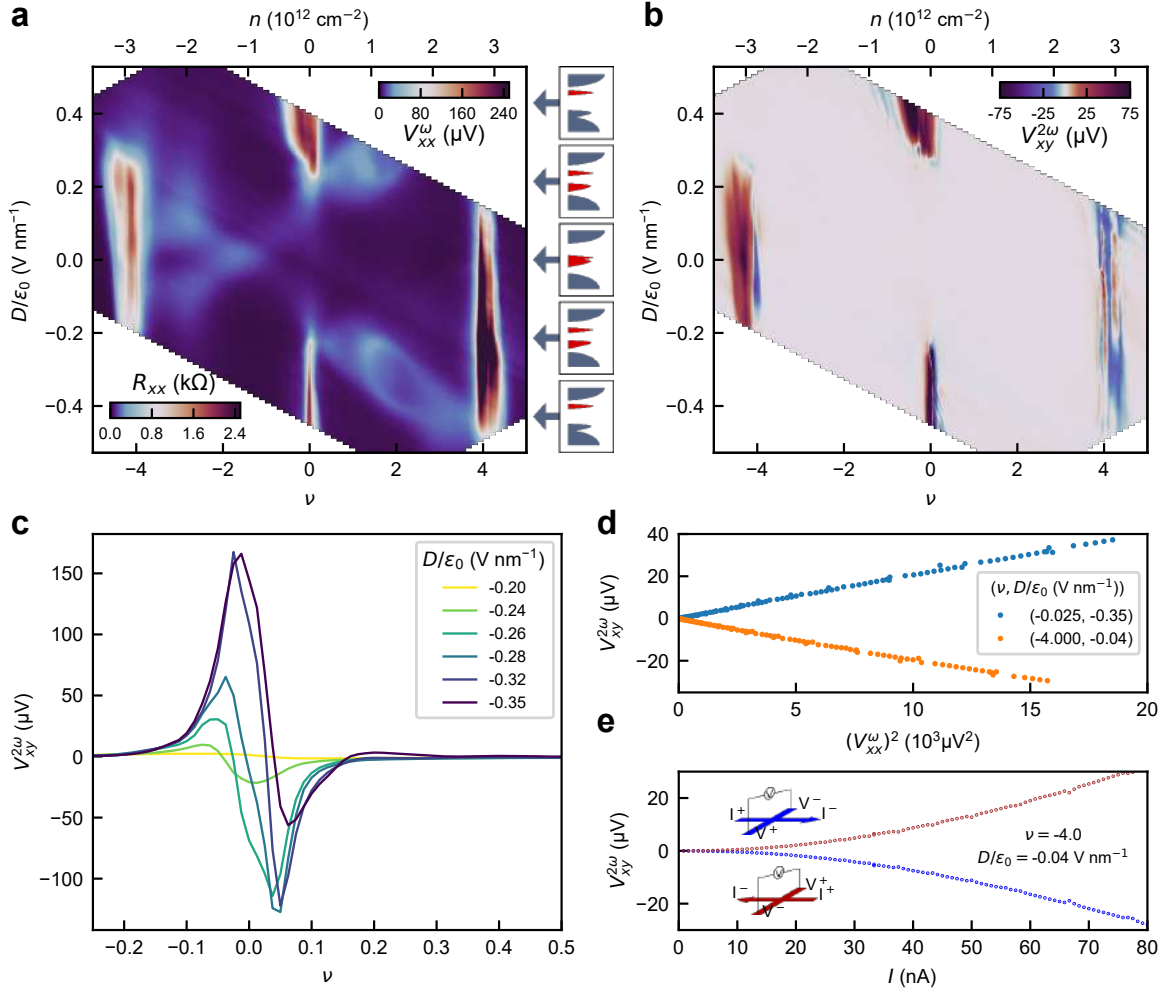


Fig. 2. Longitudinal and NLH voltages in TDBG. **a**, Longitudinal voltage (V_{xx}^{ω}) as a function of filling factor (ν) and perpendicular electric displacement field (D) measured by sending an ac current of $I = 100$ nA with frequency $\omega = 177$ Hz at a temperature of 1.5 K. The top x -axis indicates the charge density (n). The color bar provided in bottom left of **a** indicates the corresponding values of the longitudinal resistance (R_{xx}). The schematics to the right of **a** depict the cartoon band structures with energy in the y -axis and the density of states (DOS) in the x -axis for different regimes of D indicated by the arrows. The isolated flat bands are marked in red, while the dispersive moiré bands are marked in blue. **b**, Second-harmonic NLH voltage ($V_{xy}^{2\omega}$) as a function of ν and D measured simultaneously with V_{xx}^{ω} in **a**. $V_{xy}^{2\omega}$ peaks near the CNP gap and the moiré gaps. **c**, Line slices of $V_{xy}^{2\omega}$ vs. ν for different values of D . **d**, Linear dependence of $V_{xy}^{2\omega}$ on simultaneously measured $(V_{xx}^{\omega})^2$ by varying current as a parameter upto 80 nA at $T = 1.5$ K for two biasing points of (ν, D) . **e**, $V_{xy}^{2\omega}$ vs. I for $\nu = -4$ and $D/\epsilon_0 = -0.04$ V nm $^{-1}$. The colored schematics indicate the orientation of the current and the voltage terminals. $V_{xy}^{2\omega}$ reverses sign when the orientation of both the voltage probes and the current probes are flipped simultaneously indicating the second-order nature of the NLH voltage.

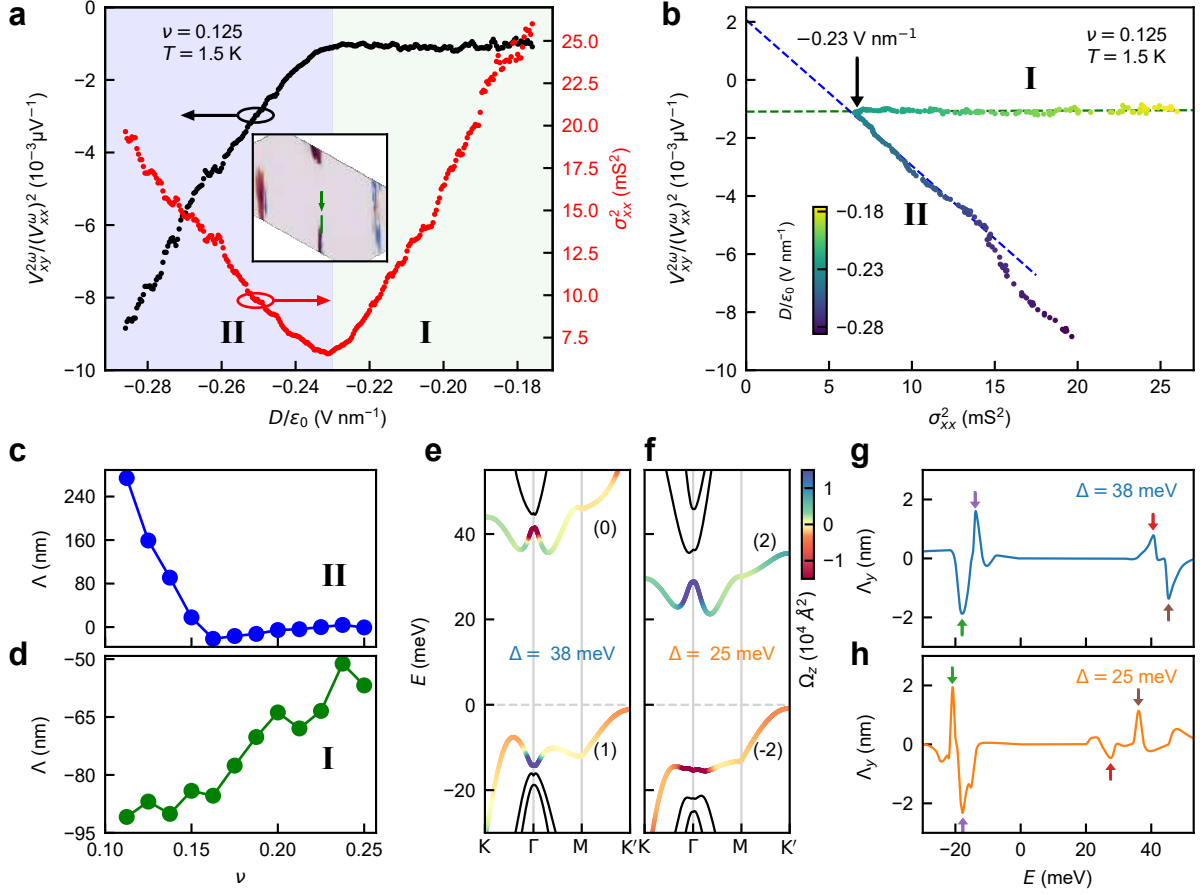


Fig. 3. Estimation of Berry curvature dipole (BCD) and its sign change across topological transition. **a**, Dependence of normalized NLH voltage $V_{xy}^{2\omega}/(V_{xx}^{\omega})^2$ (black data points, left axis) and square of longitudinal conductivity σ_{xx}^2 (red data points, right axis) on the displacement field (D). D is slowly varied at 1.5 K with the filling factor fixed at $\nu = 0.125$, which places the Fermi energy in the flat conduction band. The green vertical line pointed by the arrow in the inset of $V_{xy}^{2\omega}$ vs. ν and D (as in Fig. 2b) marks the D -range used for the plot. The valley Chern numbers of the bands change across the two regimes of D (regime-I with light-green background and regime-II with light-blue background), separated at $D/\epsilon_0 = -0.23 \text{ V nm}^{-1}$. **b**, Scaling of $V_{xy}^{2\omega}/(V_{xx}^{\omega})^2$ with σ_{xx}^2 using D as a parameter for the same ν and T as in **a**. The color of the data points indicates the corresponding D/ϵ_0 values, where D is swept at a slow rate. The vertical arrow marks the transition point between regime-I ($|D/\epsilon_0| < 0.23 \text{ V nm}^{-1}$) and regime-II ($|D/\epsilon_0| > 0.23 \text{ V nm}^{-1}$). The y -intercept of the linear fit gives the estimate of the BCD. **c**, **d**, Extracted BCD (Λ) at different values of ν close to the CNP ($\nu = 0$) for regime-II (**c**) and regime-I (**d**). The fitting error bars are smaller than the size of the individual data points. **e**, **f**, The band structures of K valley for two different values of the inter-layer potential $\Delta = 38 \text{ meV}$ (**e**) and $\Delta = 25 \text{ meV}$ (**f**). The overlaid color indicates the Berry curvature for the corresponding flat bands. The Berry curvature, and consequently, the valley Chern numbers (indicated within brackets) change across the topological transition. **g**, **h**, The corresponding variation of the calculated BCD as a function of energy (E) for $\Delta = 38 \text{ meV}$ (**g**) and $\Delta = 25 \text{ meV}$ (**h**). For a fixed band filling, the BCD changes sign across the topological transition. The green, purple, red, and brown arrows point to the sequence of the BCD peaks with the increase in E values.

merges with the remote moiré band (see Methods and Extended Data Fig. 3b, c). It is known that changes in band structure due to D lead to change in the valley Chern numbers of the bands [9, 10] which in turn should be reflected in the change in sign of the BCD [15].

To investigate the close connection of such topological transition with BCD, we first experimentally analyze the scaling between $V_{xy}^{2\omega}/(V_{xx}^\omega)^2$ and σ_{xx}^2 and later present a detailed calculation. In Fig. 3b, we find linear scaling between $V_{xy}^{2\omega}/(V_{xx}^\omega)^2$ and σ_{xx}^2 in both regime-I and regime-II. The slope of a linear $V_{xy}^{2\omega}/(V_{xx}^\omega)^2$ vs. σ_{xx}^2 dependence characterizes the contribution from skew-scattering (τ^3) process [37], while the BCD can be extracted from the y -intercept [17, 37] (see Supplementary Information section VI). A fixed temperature assures that the contributions from skew-scattering or side-jump in the NLH effect are not tuned within the linear fitted regimes [38, 39]. Interestingly, near-zero slope in regime-I suggests that the skew-scattering contribution is minimal when the flat bands are isolated from the remote moiré bands.

To distinguish the intrinsic BCD from other extrinsic contributions like side-jump, we repeat the scaling analysis for different fillings close to the band edge (see Extended Data Fig. 1). Figures 3c and 3d show the extracted BCD from regime-II and regime-I respectively. The drop in extracted BCD away from CNP ($\nu = 0$), consistent with Berry curvature hotspot peaking at the band edge, suggests that the NLH effect we observe is BCD dominated. The most striking observation, central to our study, is the sign change of BCD across the topological transition between regime-I and regime-II.

To theoretically verify the connection between BCD sign change and the topological transition, we calculate the band structure for two different values of inter-layer potential in Fig. 3e, f. A change in valley Chern number marks the topological transition. Consistently, the BCD changes sign as seen in Fig. 3h and 3g before and after the topological transition, respectively (also see Extended Data Fig. 4). We also note from Fig. 3e and 3f that the Berry curvature changes sign, around the Γ -point, across the topological

transition. Thus, the NLH effect acts as a good probe to detect topological transitions associated with the change in the valley Chern numbers [14].

We note that the BCD values in Fig. 3c, d are higher than the BCD observed in WTe₂ [17, 18]. The scaling analysis using temperature as a parameter also gives a similar magnitude of BCD (see Extended Data Fig. 2). High BCD magnitude has been theoretically predicted in strained twisted systems [15, 23, 30–32]. The origin of high BCD in graphene-based moiré systems, in the vicinity of the charge neutrality point, can be understood using the model of strained twisted bilayer graphene as a tilted Dirac system [40]. In this model, $\text{BCD} \propto t \propto \lambda^3$, where t is the tilt parameter and λ is the moiré wavelength. So, the BCD is expected to be higher in moiré materials as compared to non-moiré materials like bilayer graphene, etc. (see Supplementary Information section V for details).

Finally, we examine the variation of NLH voltage $V_{xy}^{2\omega}$ at large displacement fields and, interestingly, observe a hysteretic response as shown in Fig. 4a. Fig. 4b shows the simultaneously measured V_{xx}^ω , which also reveals hysteresis with D . The sense of hysteresis is doping dependent (see Supplementary Information section X.4) and cannot be explained by charge traps in dielectric. See Supplementary Information section X for temperature effects, rate dependence, and switching statistics of the hysteresis. The inset of Fig. 4b shows the difference in V_{xx}^ω for up and down sweeps. Intriguingly, the hysteresis is maximal around $D/\epsilon_0 = -0.23 \text{ V nm}^{-1}$ where a topological transition takes place as shown in Fig. 3b. However, more studies are required for a full microscopic understanding.

Our experimental data suggest the existence of metastable states; the origin of these states can be due to two possible mechanisms. Firstly, metastable polarization states in the system can arise from a difference in charge density across layers due to symmetry breaking in the device geometry (see Methods for further discussion). Secondly, flexoelectric coupling between perpendicular electric field and the strain gradient across the domain interfaces can lead to electric polarization in moiré systems [41]. Polarization from

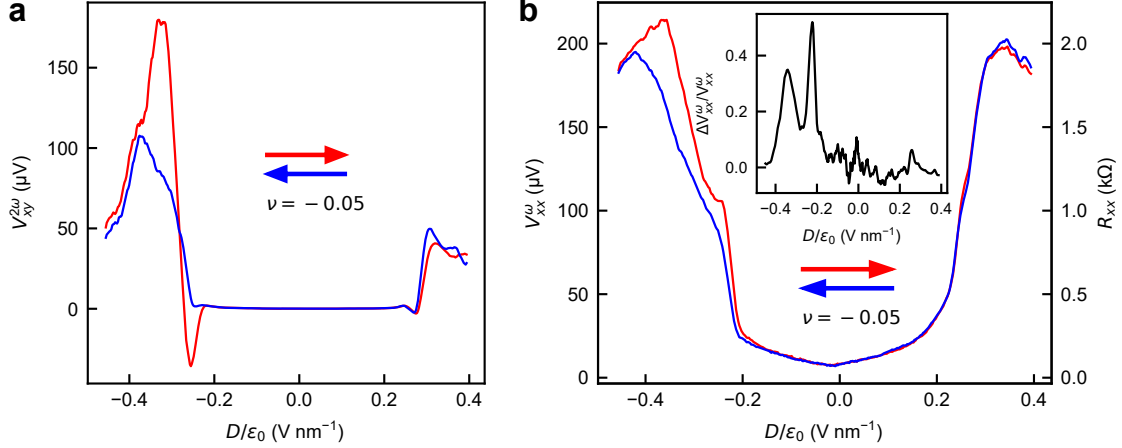


Fig. 4. Hysteresis in the NLH and longitudinal voltages. **a**, Variation of the NLH voltage $V_{xy}^{2\omega}$ with D for a filling $\nu = -0.05$ around CNP at 1.5 K. The arrows indicate the sweep direction of D/ϵ_0 . **b**, Hysteresis in V_{xx}^{ω} for up and down sweeps of D taken simultaneously with **a**. The right axis indicates the corresponding longitudinal resistance, R_{xx} . The inset shows the relative difference in V_{xx}^{ω} of up and down sweep, obtained by averaging over three consecutive data points. The relative difference is maximum around $D/\epsilon_0 = -0.23 \text{ V nm}^{-1}$. The displacement field was swept at a constant rate of $2.5 \text{ mV nm}^{-1} \text{ s}^{-1}$.

both possible mechanisms can lead to change in strain profile that can be further pinned by defects; this can account for the hysteresis we observe. Strain and polarization, through the effective electric field, modify the band structure and hence the value of V_{xx}^{ω} and $V_{xy}^{2\omega}$.

Tunable BCD values, together with the coupling of BCD to hysteresis in the same platform, as we demonstrate using TDBG, may open new frontiers for next-generation memory devices. In general, probing topological transitions using electrical transport is challenging. Our experiment demonstrates that the NLH effect can probe topological transitions. Electric field tunable band structure of few-layer heterostructures provides a useful way for probing topological transitions, as we show using TDBG. Our approach to detect topological transitions using NLH effect is applicable for 3D systems as well.

Acknowledgements:

We thank Justin Song, Abhay Pasupathy, Senthil Todadri, Biswajit Datta, Sanat Ghosh, and Supriya Mandal for helpful discussions and comments. We thank Surya Kanthi R. S., Joydip Sarkar, Krishnendu Maji, and Raghav Dhingra

for experimental assistance. M.M.D. acknowledges Nanomission grant SR/NM/NS-45/2016 and DST SUPRA SPR/2019/001247 grant along with Department of Atomic Energy of Government of India 12-R&D-TFR-5.10-0100 for support. K.W. and T.T. acknowledge support from the Elemental Strategy Initiative conducted by the MEXT, Japan (Grant Number JPMXP0112101001) and JSPS KAKENHI (Grant Numbers 19H05790 and JP20H00354). A.A. acknowledges IIT Kanpur - India, Science Engineering and Research Board (SERB)- India, and the Department of Science and Technology (DST) - India, for financial support. A.C. acknowledges the Institute Post-Doctoral fellowship of IIT Kanpur. K. Das acknowledges IIT Kanpur for Senior Research Fellowship. A.A., A.C., and K. Das also thank CC-IIT Kanpur, for the high-performance computing facility. K. Debnath is grateful to the Jawaharlal Nehru Centre for Advanced Scientific Research, India, for a research fellowship. U.V.W. acknowledges support from a JC Bose National Fellowship of SERB-DST.

Data Availability:

The experimental data used in the figures of the main text are available in Zenodo with the identifier [doi:10.5281/zenodo.5211285](https://doi.org/10.5281/zenodo.5211285) [42]. Additional data related to this study are available from the corresponding authors upon reasonable request.

Author Contributions:

S.S., P.C.A., and L.D.V.S. fabricated the devices. S.S. and P.C.A. did the measurements and analyzed the data. A.C., K. Das, and A.A. did the band structure, BCD and Chern number calculations. K. Debnath and U.V.W. did the polarization calculations. K.W. and T.T. grew the hBN crystals. S.S., P.C.A., A.A., and M.M.D. wrote the manuscript with inputs from everyone. M.M.D. supervised the project.

Competing Interests:

The authors declare no competing interests.

References

- [1] Xiao, D., Chang, M.-C. & Niu, Q. Berry phase effects on electronic properties. *Reviews of Modern Physics* **82**, 1959–2007 (2010).
- [2] Nagaosa, N., Sinova, J., Onoda, S., MacDonald, A. H. & Ong, N. P. Anomalous Hall effect. *Reviews of Modern Physics* **82**, 1539–1592 (2010).
- [3] Burg, G. W. *et al.* Correlated insulating states in twisted double bilayer graphene. *Physical Review Letters* **123**, 197702 (2019).
- [4] Shen, C. *et al.* Correlated states in twisted double bilayer graphene. *Nature Physics* **16**, 520–525 (2020).
- [5] Adak, P. C. *et al.* Tunable bandwidths and gaps in twisted double bilayer graphene on the verge of correlations. *Physical Review B* **101**, 125428 (2020).
- [6] Cao, Y. *et al.* Tunable correlated states and spin-polarized phases in twisted bilayer–bilayer graphene. *Nature* **583**, 215–220 (2020).
- [7] Liu, X. *et al.* Tunable spin-polarized correlated states in twisted double bilayer graphene. *Nature* **583**, 221–225 (2020).
- [8] Sinha, S. *et al.* Bulk valley transport and Berry curvature spreading at the edge of flat bands. *Nature Communications* **11**, 5548 (2020).
- [9] Koshino, M. Band structure and topological properties of twisted double bilayer graphene. *Physical Review B* **99**, 235406 (2019).
- [10] Zhang, Y.-H., Mao, D., Cao, Y., Jarillo-Herrero, P. & Senthil, T. Nearly flat Chern bands in moiré superlattices. *Physical Review B* **99**, 075127 (2019).
- [11] Fu, L. & Sodemann, I. Quantum nonlinear Hall effect induced by Berry curvature dipole in time-reversal invariant materials. *Physical Review Letters* **115**, 216806 (2015).
- [12] Ma, Q., Grushin, A. G. & Burch, K. S. Topology and geometry under the nonlinear electromagnetic spotlight. *Nature Materials* **20**, 1601–1614 (2021).
- [13] Du, Z. Z., Lu, H.-Z. & Xie, X. C. Nonlinear Hall effects. *Nature Reviews Physics* **3**, 744–752 (2021).
- [14] Facio, J. I. *et al.* Strongly enhanced Berry dipole at topological phase transitions in BiTeI. *Physical Review Letters* **121**, 246403 (2018).
- [15] Hu, J.-X., Zhang, C.-P., Xie, Y.-M. & Law, K. T. Nonlinear Hall effects in strained twisted bilayer WSe₂. *arXiv:2004.14140 [cond-mat]* (2020).
- [16] Song, J. C. W., Samutpraphoot, P. & Levitov, L. S. Topological Bloch bands in graphene superlattices. *Proceedings of the*

- National Academy of Sciences* **112**, 10879–10883 (2015).
- [17] Kang, K., Li, T., Sohn, E., Shan, J. & Mak, K. F. Nonlinear anomalous Hall effect in few-layer WTe₂. *Nature Materials* **18**, 324–328 (2019).
- [18] Ma, Q. *et al.* Observation of the nonlinear Hall effect under time-reversal-symmetric conditions. *Nature* **565**, 337–342 (2019).
- [19] Shvetsov, O. O., Esin, V. D., Timonina, A. V., Kolesnikov, N. N. & Deviatov, E. V. Nonlinear Hall effect in three-dimensional Weyl and Dirac semimetals. *JETP Letters* **109**, 715–721 (2019).
- [20] Xiao, J. *et al.* Berry curvature memory through electrically driven stacking transitions. *Nature Physics* **16**, 1028–1034 (2020).
- [21] Tiwari, A. *et al.* Giant c-axis nonlinear anomalous Hall effect in T_d-MoTe₂ and WTe₂. *Nature Communications* **12**, 2049 (2021).
- [22] Ho, S.-C. *et al.* Hall effects in artificially corrugated bilayer graphene without breaking time-reversal symmetry. *Nature Electronics* **4**, 116–125 (2021).
- [23] Huang, M. *et al.* Giant nonlinear Hall effect in twisted WSe₂. *arXiv:2006.05615 [cond-mat]* (2021).
- [24] Kim, K. *et al.* Tunable moiré bands and strong correlations in small-twist-angle bilayer graphene. *Proceedings of the National Academy of Sciences* **114**, 3364–3369 (2017).
- [25] Cao, Y. *et al.* Correlated insulator behaviour at half-filling in magic-angle graphene superlattices. *Nature* **556**, 80–84 (2018).
- [26] Cao, Y. *et al.* Unconventional superconductivity in magic-angle graphene superlattices. *Nature* **556**, 43–50 (2018).
- [27] Lu, X. *et al.* Superconductors, orbital magnets and correlated states in magic-angle bilayer graphene. *Nature* **574**, 653–657 (2019).
- [28] Sharpe, A. L. *et al.* Emergent ferromagnetism near three-quarters filling in twisted bilayer graphene. *Science* **365**, 605–608 (2019).
- [29] Serlin, M. *et al.* Intrinsic quantized anomalous Hall effect in a moiré heterostructure. *Science* **367**, 900–903 (2020).
- [30] Zhang, C.-P. *et al.* Giant nonlinear Hall effect in strained twisted bilayer graphene. *arXiv:2010.08333 [cond-mat]* (2020).
- [31] Pantaleón, P. A., Low, T. & Guinea, F. Tunable large Berry dipole in strained twisted bilayer graphene. *Physical Review B* **103**, 205403 (2021).
- [32] He, Z. & Weng, H. Giant nonlinear Hall effect in twisted bilayer WTe₂. *npj Quantum Materials* **6**, 101 (2021).
- [33] He, M. *et al.* Symmetry breaking in twisted double bilayer graphene. *Nature Physics* **17**, 26–30 (2021).
- [34] Chebrolov, N. R., Chittari, B. L. & Jung, J. Flat bands in twisted double bilayer graphene. *Physical Review B* **99**, 235417 (2019).
- [35] McGilly, L. J. *et al.* Visualization of moiré superlattices. *Nature Nanotechnology* **15**, 580–584 (2020).
- [36] Kazmierczak, N. P. *et al.* Strain fields in twisted bilayer graphene. *Nature Materials* **20**, 956–963 (2021).
- [37] He, P. *et al.* Quantum frequency doubling in the topological insulator Bi₂Se₃. *Nature Communications* **12**, 698 (2021).
- [38] Xiao, C., Zhou, H. & Niu, Q. Scaling parameters in anomalous and nonlinear Hall effects depend on temperature. *Physical Review B* **100**, 161403 (2019).

- [39] Du, Z. Z., Wang, C. M., Li, S., Lu, H.-Z. & Xie, X. C. Disorder-induced nonlinear Hall effect with time-reversal symmetry. *Nature Communications* **10**, 3047 (2019).
- [40] Mannaï, M. & Haddad, S. Twistronics versus straintronics in twisted bilayers of graphene and transition metal dichalcogenides. *Physical Review B* **103**, L201112 (2021).
- [41] Li, Y. *et al.* Unraveling strain gradient induced electromechanical coupling in twisted double bilayer graphene moiré superlattices. *Advanced Materials* **33**, 2105879 (2021).
- [42] Sinha, S. *et al.* Experimental data for Berry curvature dipole senses topological transition in a moiré superlattice. *Zenodo* (2021).

METHODS

1 Device fabrication

We fabricate multiple dual gated TDBG devices. We have a metal top gate and SiO_2 (~ 280 nm)/ Si^{++} back gate. Dual gates allow us to independently control the charge density (n) and the perpendicular displacement field (D), where $n = (C_{BG}V_{BG} + C_{TG}V_{TG})/e$ and $D = (C_{BG}V_{BG} - C_{TG}V_{TG})/2$. Here, C_{BG} (C_{TG}) is the back (top) gate capacitance and V_{BG} (V_{TG}) is the voltage applied to the back (top) gate, respectively. e is the electronic charge. To prepare the hBN/TDBG/hBN graphene stacks, we pre-cut bilayer graphene using a tapered optical fiber scalpel [1]. The detail fabrication and twist angle determination procedure is discussed in the methods of Ref. [8]. The twist angle is additionally confirmed via magneto-transport measurements.

2 Measurement technique

We send current using DS360 ultra-low distortion function generator. The chosen frequency for all the data is 177 Hz, except for Supplementary Fig. 8 where we vary the frequency. The voltages, V_{xx}^ω and $V_{xy}^{2\omega}$, are measured using SR830 lock-in amplifier in the first harmonic and second harmonic mode, respectively. In addition, to measure the DC voltage (Supplementary Fig. 20) generated due to the NLH effect, we use Keithley 2182 nanovoltmeter. For applying DC voltages to the top and back gate, we use NI DAQ. The temperature is measured using a sensor placed close to the device. The findings reported in the main manuscript are from a TDBG device with twist angle 1.10° ; other devices are shown in Supplementary Fig. 5 and 16.

3 BCD estimation

3.1 Using electric field as parameter

To extract out the BCD (Λ), we use the formula $\frac{E_\perp^{2\omega}}{(E_\parallel)^2} = \xi\sigma_{xx}^2 + \eta$, where $E_\perp^{2\omega}$ is the second-order nonlinear electric field, E_\parallel is the in-plane longitudinal electric field, parallel to the direction of current, ξ is the slope and η is the intercept. Using the fact that the length and width of our device are $2 \mu\text{m}$ each, $\eta = 2 \times y$ -intercept of $\frac{V_{xy}^{2\omega}}{(V_{xx}^\omega)^2}$ vs. σ_{xx}^2 dependence. We fit the D -parametric plot of $\frac{V_{xy}^{2\omega}}{(V_{xx}^\omega)^2}$ vs. σ_{xx}^2 with a linear dependence (see Supplementary Information section VI for details) to extract η and use the relation $\Lambda = \eta \frac{E_F}{\pi e}$ to estimate the BCD [17]. We assume that E_F is $\sim 1\%$ (limited by the energy scale $k_B T$ set by the temperature $T = 1.5$ K) of the bandwidth (~ 10 meV) of the flat band. To ensure that we place the Fermi energy E_F within the flat band and not at the gap, we measure the temperature dependence of R_{xx} and find a metallic behavior irrespective of the chosen value of D (see Extended Data Fig. 3a).

To verify the robustness of our observation of BCD sign change, we systematically show the scaling of normalized nonlinear Hall voltage ($V_{xy}^{2\omega}/(V_{xx}^\omega)^2$) with square of longitudinal conductivity (σ_{xx}^2) for three different fillings (ν) in Extended Data Fig. 1. Extended Data Fig. 1a, d, and g shows the measured nonlinear Hall voltage $V_{xy}^{2\omega}$ and longitudinal voltage V_{xx}^ω as a function of the displacement field for three different ν . The background color denotes the two regimes— regime-I and regime-II, across which a topological transition occurs. We see broad peaks in V_{xx}^ω across the critical electric field of $D/\epsilon_0 = -0.23$ V nm $^{-1}$ in all three cases. Using the measured V_{xx}^ω and $V_{xy}^{2\omega}$ as in Extended Data Fig. 1a, d, and g, we plot the corresponding normalized NLH voltage

$V_{xy}^{2\omega}/(V_{xx}^\omega)^2$ and $\sigma_{xx}^2 = (I/V_{xx}^\omega)^2$ as a function of displacement field for the three fillings in Extended Data Fig. 1b, e, and h. In Extended Data Fig. 1c, f, and i, we plot $V_{xy}^{2\omega}/(V_{xx}^\omega)^2$ vs. σ_{xx}^2 , using displacement field as a parameter. The displacement field ($D/\epsilon_0 = -0.23 \text{ V nm}^{-1}$), at which the change in sign of intercept occurs, remains invariant for different fillings. We extract the intercept and use it to estimate BCD as described above, and plot in Fig. 3c and 3d of the main manuscript.

The extracted BCD values from the two regimes are opposite in sign. A characteristic signature of a topological transition is a change in sign of BCD, as discussed in the main manuscript and also in Ref. [15] and Ref. [14]. As we show via resistance vs. temperature measurements in Extended Data Fig. 3c, displacement field closes the hole-side moiré gap around the same $D/\epsilon_0 = -0.23 \text{ V nm}^{-1}$. Displacement field, that causes the flat bands to touch the remote moiré valence bands, changes the valley Chern number of the bands in TDBG [9, 10], as we independently show in our calculations (Fig. 3e,f of the main manuscript) for the twist angle of 1.1° . Such a change in sign of valley Chern number accounts for the two linear regimes with different signs of intercepts.

3.2 Using temperature as parameter

To independently confirm the order of magnitude of the estimated BCD, we also study the temperature dependence of the NLH voltage. In Extended Data Fig. 2, we show the scaling of normalized nonlinear Hall voltage ($V_{xy}^{2\omega}/(V_{xx}^\omega)^2$) with the square of longitudinal conductivity (σ_{xx}) for the filling $\nu = 0.125$ (the same ν for which we show a linear scaling, using displacement field as a parameter, in Fig. 3b of the main manuscript) and displacement field $D/\epsilon_0 = -0.25 \text{ V nm}^{-1}$. In Extended Data Fig. 2a, we show the temperature dependence of the NLH voltage $V_{xy}^{2\omega}$ (blue-colored data points) and longitudinal voltage V_{xx}^ω (orange-colored data points). We see that $V_{xy}^{2\omega}$ goes close to zero at $\sim 20 \text{ K}$. In Extended Data Fig. 2b, we plot the temperature dependence of $V_{xy}^{2\omega}/(V_{xx}^\omega)^2$ (black data points) and σ_{xx}^2 (red data points), using the data in Extended Data Fig. 2a. A decreasing σ_{xx}^2 with increasing temperature suggests that the filling $\nu = 0.125$ corresponds to placing the Fermi level in the conduction flat band. In Extended Data Fig. 2c, we plot $V_{xy}^{2\omega}/(V_{xx}^\omega)^2$ vs. σ_{xx}^2 , using temperature as a parameter and find similar linear dependence, as reported earlier [17], till $T = 7 \text{ K}$. The temperature regime is less than the Bloch-Grüneisen temperature, ensuring that the other extrinsic contributions are not tuned in this temperature regime. A similar magnitude of y -intercept in $V_{xy}^{2\omega}/(V_{xx}^\omega)^2$ as in Fig. 3b of the main manuscript, suggests that BCD using temperature as a parameter is of similar magnitude that we get from parametric scaling of D .

4 Inferring band structure using R vs. T dependence

In Extended Data Fig. 3, we show the temperature (T) variation of longitudinal resistance (R_{xx}) for fillings at $\nu = 0$ (corresponding to CNP in Extended Data Fig. 3b), $\nu = 0.125$ (corresponding to conduction flat band edge in Extended Data Fig. 3a) and $\nu = -4$ (corresponding to hole-side moiré gap in Extended Data Fig. 3c) at different displacement fields (D). In Extended Data Fig. 3b, we see that as the magnitude of displacement field is increased, the slope of R_{xx} vs. T changes from positive to negative, indicating a gap opening at CNP at a displacement field around $|D|/\epsilon_0$ of 0.2 V nm^{-1} . This establishes that in regime-I, a gap at CNP persists between the red colored flat bands.

In Extended Data Fig. 3c, we see that as the magnitude of displacement field is increased, the slope of R_{xx} vs. T changes from negative to positive, indicating a gap closing at the hole-side moiré gap at $\nu = -4$ at a displacement field around $|D|/\epsilon_0$ of 0.23 V nm^{-1} . This establishes that in regime-II, the hole-side moiré gap is closed and the flat band has merged with the hole-side remote moiré band.

5 Berry curvature dipole and topological transition

To investigate the topological phase-transition and associated sign reversal of Berry curvature dipole we have followed the low-energy continuum model approach of Bistritzer and MacDonald [2] for twisted bilayer graphene and extended it to TDBG (see Supplementary Information section I for details). The perpendicular electric field tunability of electronic band structure has been included in the Hamiltonian by a parameter Δ , which represents constant potential gradient across the layers. The presence of finite strain in the fabricated TDBG sample breaks the C_3 symmetry (see Fig. 1a) which causes non-zero BCD. The uniaxial strain has been introduced into our model Hamiltonian as [3]

$$\mathcal{E} = \epsilon \begin{pmatrix} -\cos^2 \phi + \nu \sin^2 \phi & -(1 + \nu) \sin \phi \cos \phi \\ -(1 + \nu) \sin \phi \cos \phi & -\sin^2 \phi + \nu \cos^2 \phi \end{pmatrix}, \quad (2)$$

where a strain of magnitude ϵ is applied along a direction making angle ϕ with the zigzag direction of graphene. ν , the Poisson's ratio is equal to ~ 0.16 for graphene. For our calculations, we have considered strain along the zigzag direction ($\phi = 0^\circ$).

In Extended Data Fig. 4, we have plotted BCD as a function of inter-layer potential (Δ) and chemical potential (μ) at a fixed strain value of 0.1%. The butterfly structure signifies the evolution of BCD with the perpendicular electric field. The sign reversal of BCD near critical inter-layer potential $\Delta = 34$ meV indicates a topological transition. The upper panel of Extended Data Fig. 4 shows the y -component of BCD in the conduction band side ($\mu > 0$). Before phase-transition, at 25 meV and 30 meV, the red lobe signifies the negative BCD for the first conduction band while the blue lobe represents positive BCD for moiré conduction bands. The corresponding band dispersions are shown in Extended Data Fig. 4b, c. The overlaid color indicates the Berry curvature hot spots within the band. After the phase-transition, at $\Delta = 38$ and 43 meV, we observe positive lobe of BCD for the first conduction band while negative lobe for the higher conduction band. The corresponding dispersions are shown in Extended Data Fig. 4d, e. From the color map of Berry curvature, it is evident that in regime-I (before transition), the valence (conduction) band has a negative (positive) Berry curvature hotspot while it gets reversed in regime-II (after transition).

6 Metastable states in h-BN encapsulated twisted double bilayer graphene

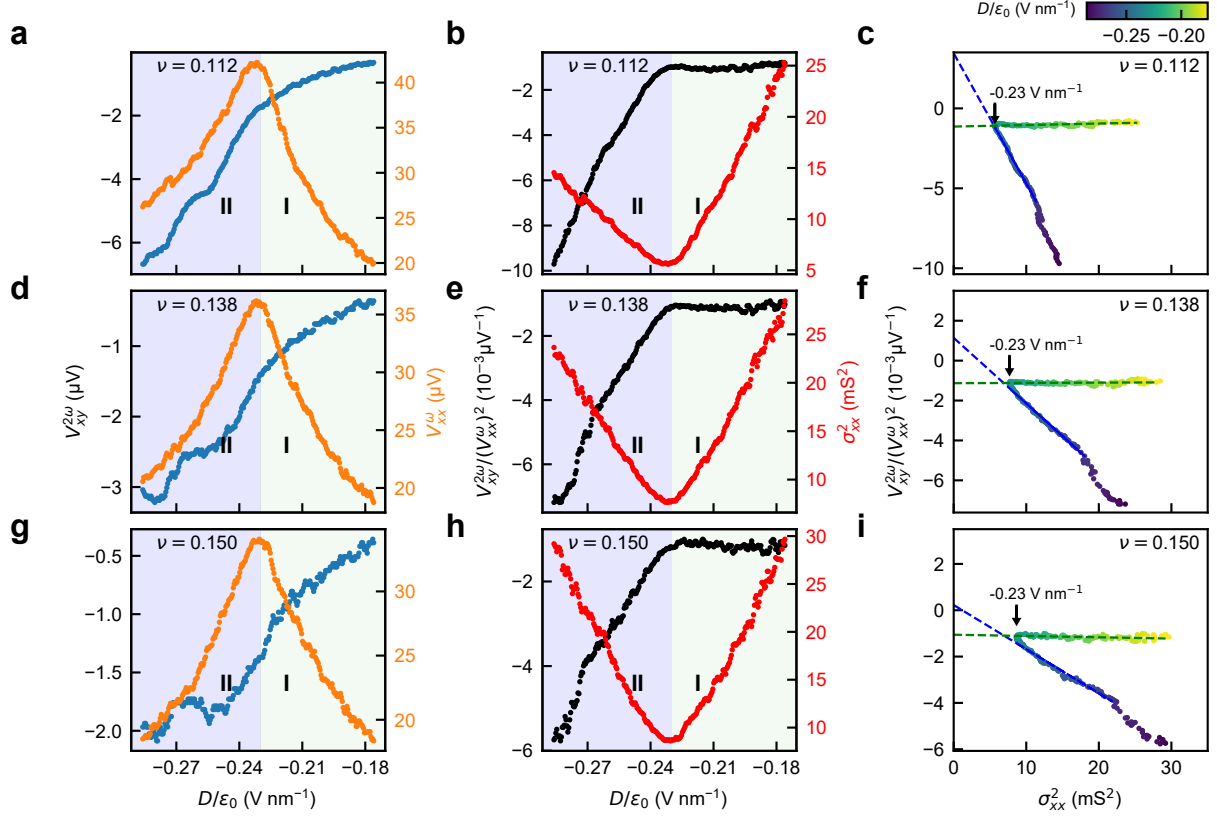
To identify the metastable states that possibly cause the observed hysteresis, we first present first-principles density functional theory analysis of a Gr-Gr-h-BN trilayer, which constitutes one of the halves which are twisted by a small angle in the TDBG. Interestingly, the outer h-BN monolayer breaks the sublattice-symmetry opening up a small gap at the Fermi level (see Extended Data Fig. 5a), accompanied by a weak layer asymmetry in the constitution of frontier electronic states (bands of p_z orbitals) reflecting on an accumulation of a small electronic charge on one of the two graphene monolayers. This is expected from the lack of inversion or horizontal reflection symmetries in the trilayer, and our estimate of its polarization (along the z -axis) is $-0.34 \mu\text{C}/\text{cm}^2$. We analyze effects of perpendicular electric field on the TDBG in two steps, focusing first on the coupling of field with the DBG (twist angle = 0) and then discuss the effect of twist in terms of variation in stacking between the DBGs. Using a rigid band model of frontier electronic states of DBG (for details of rigid band model refer to Supplementary Information section XI), we demonstrate that electric field permits switching to two metastable states with opposite polarization (Extended Data Fig. 5d) arising from the inversion of frontier electronic states in one of the DBGs (see Extended Data Fig. 5c). However, these states are symmetry equivalent and would not explain the hysteresis observed in

resistances of TDBG, which we argue to arise from two mechanisms: (a) the inhomogeneous doping across the layers in the TDBG due to differences in the top and bottom doping as evident in our calculations of gated TDBG with a twist angle of 21.78° , and (b) switchable ferroelectric polarization associated with redistribution of regions with different stacking sequences (AA versus AB) across the twisted layers as shown in [4].

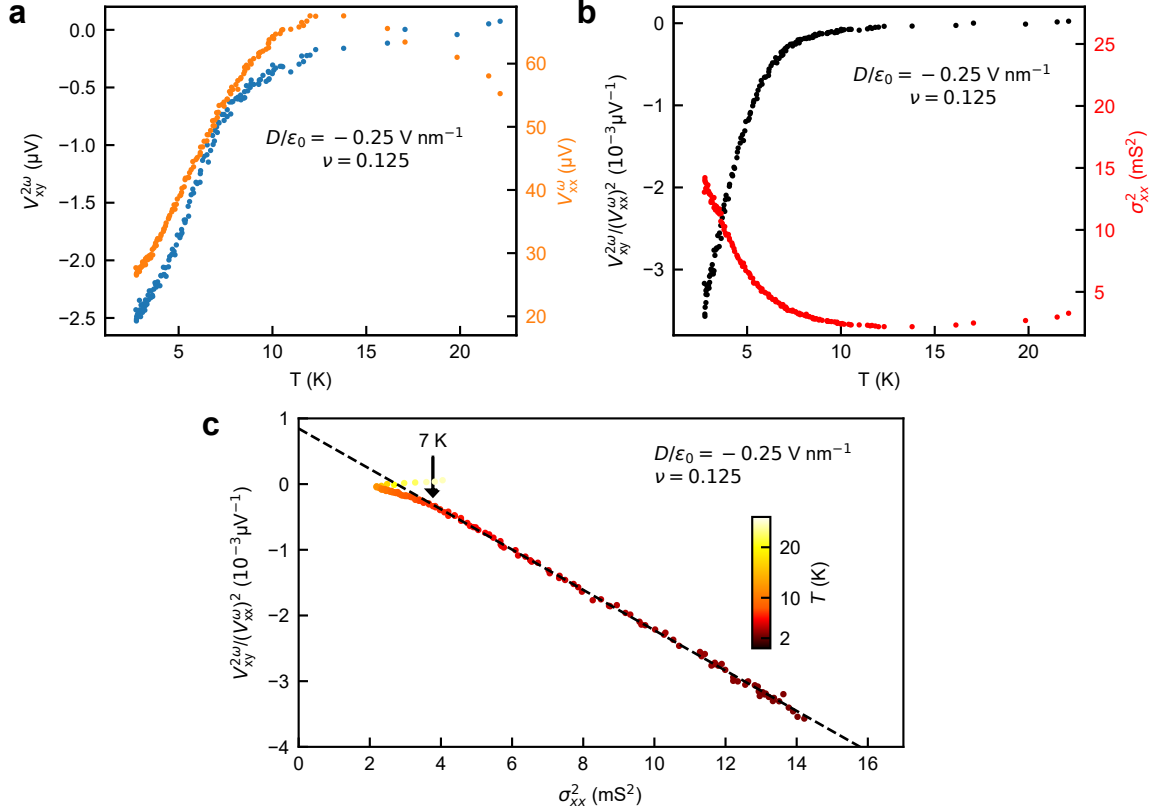
Our calculations of the TDBG (with 21.78°) with a bottom gate reveals the development of polarization upon doping with an estimate of $0.6 \mu\text{C}/\text{cm}^2$ (refer to Supplementary Fig. 19a). This is comparable to $P \sim 0.68 \mu\text{C}/\text{cm}^2$ of bilayered h-BN [4] and larger than that ($P \sim -0.18 \mu\text{C}/\text{cm}^2$) arising from the restructuring in terms of stacking sequence [5] in heterostructures. Thus, the observed hysteresis has possible contributions from inhomogeneous stacking as well as inhomogeneous, layer-dependent carrier concentration.

References

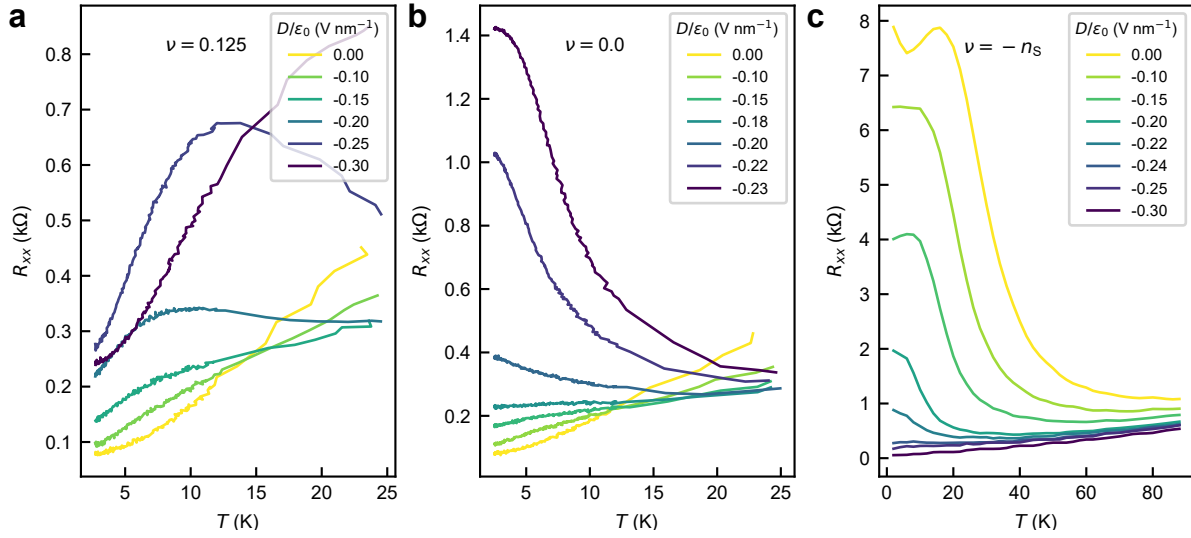
- [1] Varma Sangani, L. D. *et al.* Facile deterministic cutting of 2D materials for twistrionics using a tapered fibre scalpel. *Nanotechnology* **31**, 32LT02 (2020).
- [2] Bistritzer, R. & MacDonald, A. H. Moiré bands in twisted double-layer graphene. *Proceedings of the National Academy of Sciences* **108**, 12233–12237 (2011).
- [3] He, W.-Y., Goldhaber-Gordon, D. & Law, K. T. Giant orbital magnetoelectric effect and current-induced magnetization switching in twisted bilayer graphene. *Nature Communications* **11**, 1650 (2020).
- [4] Yasuda, K., Wang, X., Watanabe, K., Taniguchi, T. & Jarillo-Herrero, P. Stacking-engineered ferroelectricity in bilayer boron nitride. *Science* **372**, 1458–1462 (2021).
- [5] Zheng, Z. *et al.* Unconventional ferroelectricity in moiré heterostructures. *Nature* **588**, 71–76 (2020).



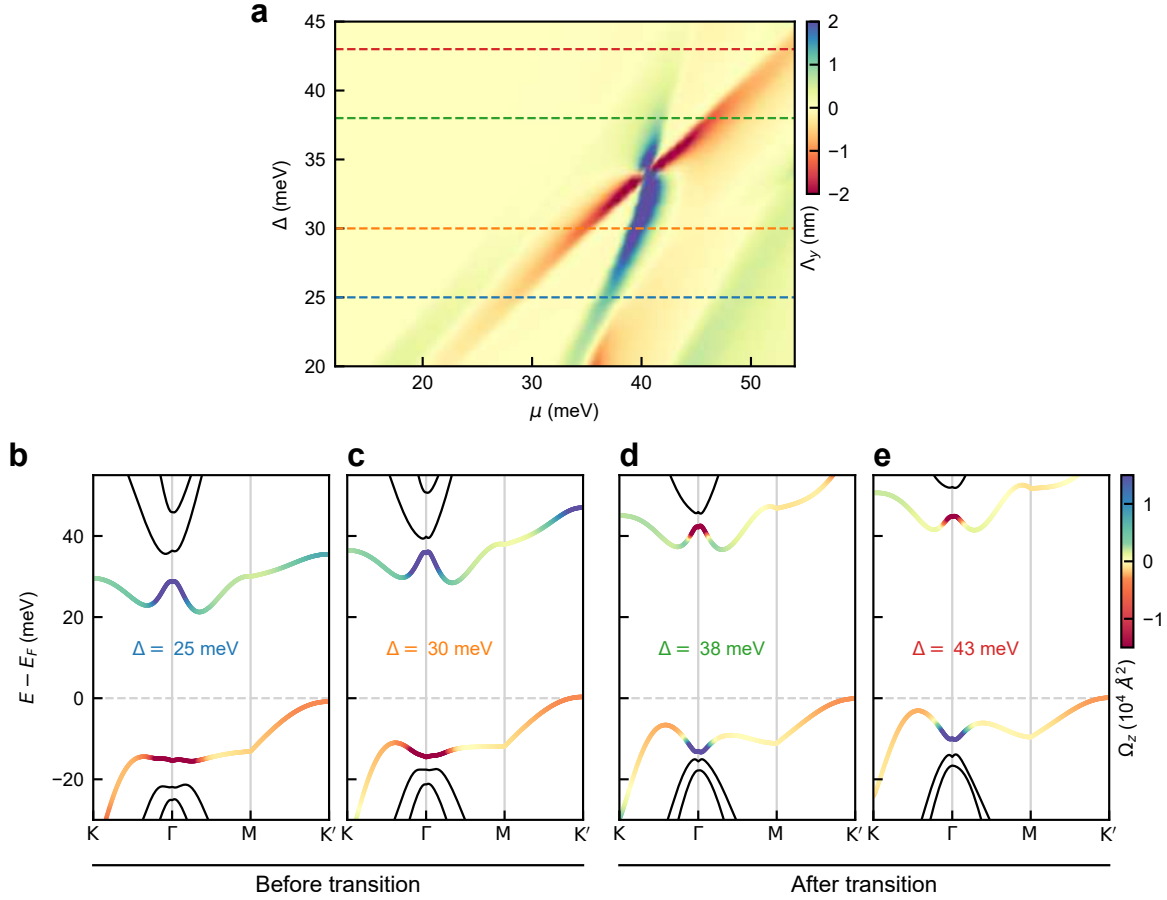
Extended Data Fig. 1. Scaling of normalized nonlinear Hall voltage $V_{xy}^{2\omega}/(V_{xx}^\omega)^2$ with the square of longitudinal conductivity (σ_{xx}^2) for different fillings ν with displacement field as parameter. **a, d, g, The variation of nonlinear Hall voltage $V_{xy}^{2\omega}$ (blue-colored data points corresponding to the left axis) and longitudinal voltage V_{xx}^ω (orange-colored data points corresponding to the right axis) as a function of the displacement field D/ϵ_0 for three different fillings. **b, e, h**, The corresponding variation of normalized nonlinear Hall voltage $V_{xy}^{2\omega}/(V_{xx}^\omega)^2$ (black colored data points corresponding to the left axis) and square of longitudinal conductivity σ_{xx}^2 (red-colored data points corresponding to the right axis) as a function of the displacement field D/ϵ_0 , extracted for the same fillings used in **a, g** and **d**, respectively. **c, f, i**, The variation of normalized nonlinear Hall voltage $V_{xy}^{2\omega}/(V_{xx}^\omega)^2$ with square of longitudinal conductivity σ_{xx}^2 plotted parametrically as a function of the displacement field D/ϵ_0 , using **b, e** and **h**, respectively. The displacement field value of data points in V nm^{-1} is indicated by the color bar (shown in top right). The dashed green line and dashed blue line indicate fits to linear scaling in regime-I and regime-II respectively, used to extract BCD. The fillings shown here are $\nu = 0.112$ (**a-c**), 0.138 (**d-f**) and 0.150 (**g-i**). The light green background and light blue background correspond to regime-I and regime-II, respectively, as discussed in Fig. 3a of the main manuscript. The measurements were performed using a current of 100 nA with a frequency of 177 Hz at a temperature of 1.5 K.**



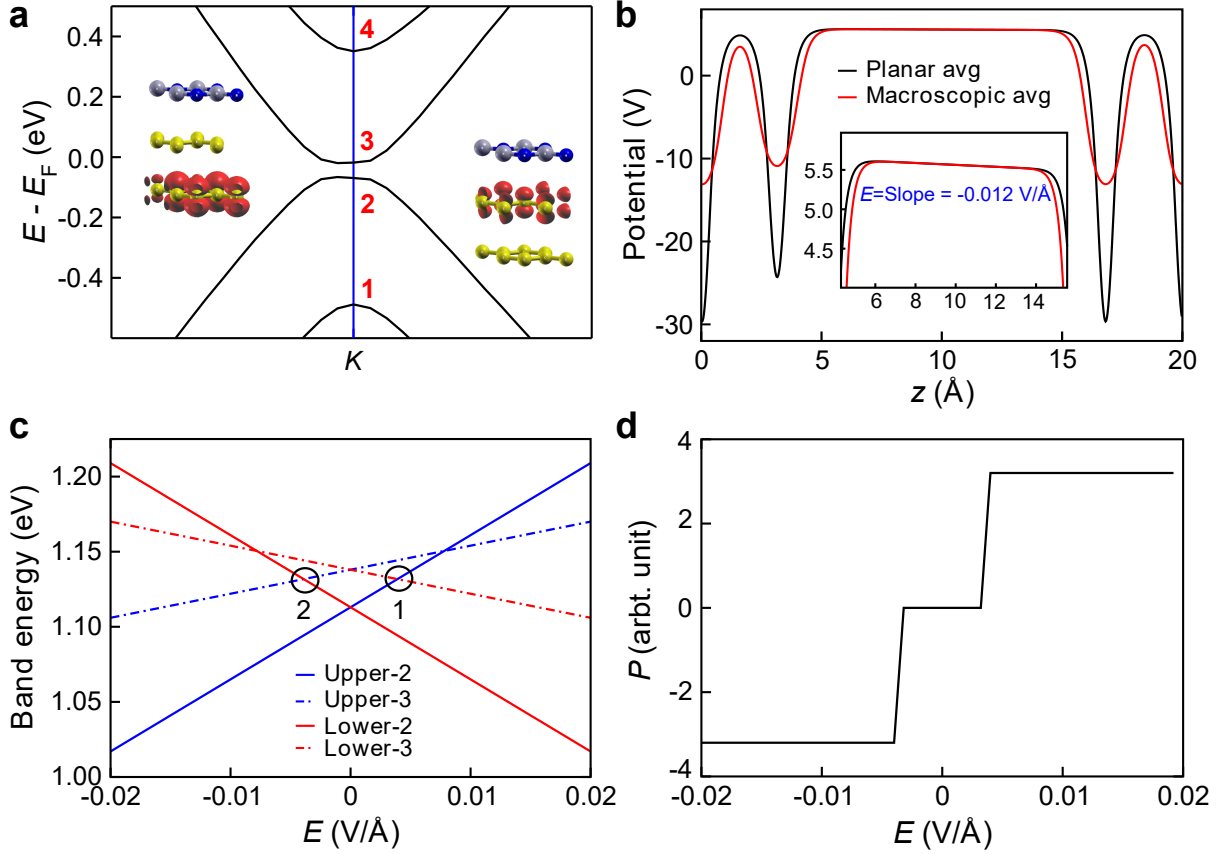
Extended Data Fig. 2. Scaling of normalized nonlinear Hall voltage $V_{xy}^{2\omega}/(V_{xx}^\omega)^2$ with square of longitudinal conductivity (σ_{xx}^2) with temperature as parameter. **a**, The variation of nonlinear Hall voltage $V_{xy}^{2\omega}$ (blue-colored data points corresponding to the left axis) and longitudinal voltage V_{xx}^ω (orange-colored data points corresponding to the right axis) as a function of temperature T for $\nu = 0.125$. **b**, The corresponding variation of normalized nonlinear Hall voltage $V_{xy}^{2\omega}/(V_{xx}^\omega)^2$ (black-colored data points corresponding to the left axis) and square of longitudinal conductivity σ_{xx}^2 (red-colored data points corresponding to the right axis) as a function of T , extracted for the same filling used in **a**. **c**, The variation of $V_{xy}^{2\omega}/(V_{xx}^\omega)^2$ with σ_{xx}^2 plotted parametrically as a function of T , using the results in **b**. The temperature value of data points in Kelvin is indicated by the color. The dashed line indicates a linear fit till 7 K.



Extended Data Fig. 3. Variation of longitudinal resistance with temperature. a-c, Variation of longitudinal resistance R_{xx} with temperature T for filling $\nu = 0.125$ (a), $\nu = 0$ (b) and $\nu = -4$ (c). The color of the line-plots indicates the corresponding displacement field.



Extended Data Fig. 4. Evolution of Berry curvature dipole (BCD). **a**, Dependence of the y -component of BCD on the chemical potential (μ) and inter-layer potential (Δ) at the conduction band side. **b**, **c**, Energy dispersion along high symmetry k -paths for $\Delta = 25$ meV (**b**) and $\Delta = 30$ meV (**c**) before transition. **d**, **e**, Similar energy dispersion for $\Delta = 38$ meV (**d**) and $\Delta = 43$ meV (**e**) after transition. The color map shows the Berry curvature value for the flat bands.



Extended Data Fig. 5. Metastable states and polarization in TDBG. **a**, Electronic structure of Gr-Gr-h-BN shows a band gap of 26 meV at K point. The inset shows the spatial distribution of the wave functions of bands labelled 2 and 3. **b**, Electric field (E) calculated from the slope of the average macroscopic potential of Gr-Gr-h-BN in vacuum. **c**, Evolution and crossing of band 2 and 3 at $E = -0.0039$ V/Å and $E = 0.0039$ V/Å of upper and lower trilayer of h-BN-TDBG-h-BN as a function of electric field using our rigid band model. **d**, metastable states for (i) $E < -0.0039$ V/Å and (ii) $E > 0.0039$ V/Å, with nonzero polarization in h-BN-TDBG-h-BN that are accessible with the electric field.

Supplementary Information

I Moiré flat bands in TDBG

To obtain the electronic band structure and related topological properties of the AB-AB twisted double bilayer graphene (TDBG) with twist angle 1.1° we follow the continuum model approach of Bistritzer and MacDonald [1]. The AB-AB TDBG can be fabricated by placing two AB-stacked bilayer graphene (see the side view in Supplementary Fig. S1a) on top of each other and rotate the bilayers with respect to each other. For the band structure calculation, we assume that the upper bilayer ($l = 1$) is rotated by an angle $\theta/2$ and the lower bilayer ($l = 2$) is rotated by an angle $-\theta/2$ adding to total twist angle θ . The smallest continuum Hamiltonian near the \mathbf{K} valley can be written as [34]

$$H = \begin{pmatrix} h_t^+ + \Delta_t^+ & t_k^+ & 0 & 0 \\ t_k^{+\dagger} & h_b^+ + \Delta_b^+ & T(\mathbf{r}) & 0 \\ 0 & T(\mathbf{r})^\dagger & h_t^- + \Delta_t^- & t_k^- \\ 0 & 0 & t_k^{-\dagger} & h_b^- + \Delta_b^- \end{pmatrix}. \quad (\text{S1})$$

Here, $+$ ($-$) sign stands for the $l = 1$ (2) bilayer and $t(b)$ represents the top (bottom) layer of each bilayer. Due to rotation, the Dirac Hamiltonian modifies as $h^\pm = R(\mp\theta/2)\hbar v_F \mathbf{k} \cdot \sigma$, where \mathbf{k} is the crystal momentum near the valley and $\sigma = (\sigma_x, \sigma_y)$ are the Pauli matrices representing the sublattice degree of freedom of single-layer graphene. The effect of dimer site potential on each layer of a bilayer has been captured in the Hamiltonian by a parameter δ as $h_{(t/b)} = \hbar v_F \sigma \cdot \mathbf{k} + \delta(\mathcal{K} \mp \sigma_z)/2$. The inter-layer coupling matrix t_k within each bilayer is represented as

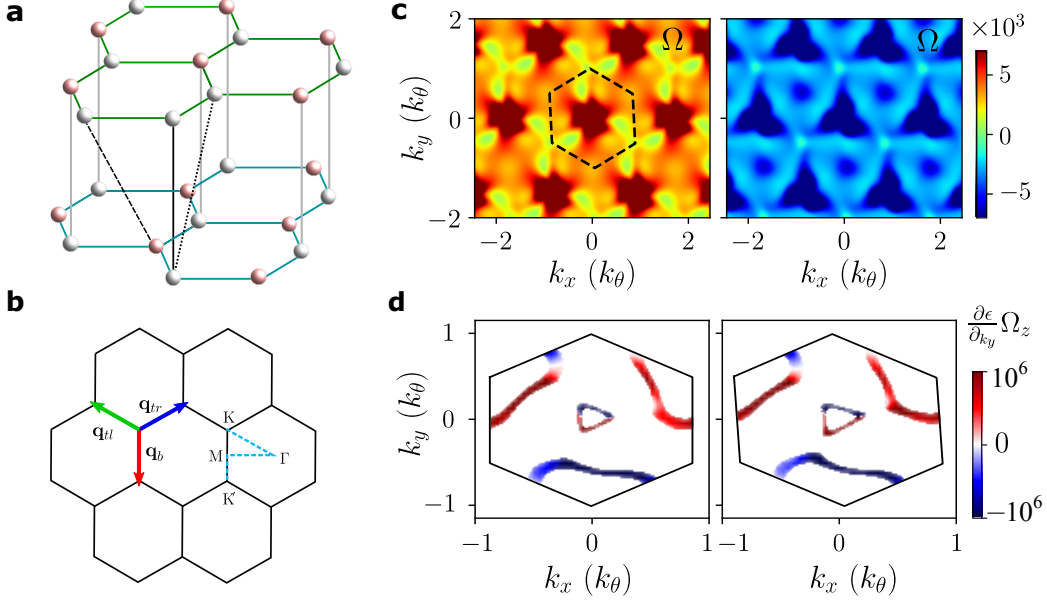
$$t_k = \begin{pmatrix} -\hbar v_4 \pi^\dagger & -\hbar v_3 \pi \\ \gamma_1 & -\hbar v_4 \pi^\dagger \end{pmatrix},$$

where $\pi = k_x + ik_y$. The strong inter-layer coupling between the two dimer sites is denoted by γ_1 (shown by solid line in Supplementary Fig. S1a), the inter-layer hopping between two non-dimer sites is denoted by v_3 (shown by dashed line in Supplementary Fig. S1a) and the inter-layer hopping between dimer and non-dimer sites is denoted by v_4 (shown by dotted line in Supplementary Fig. S1a). The various velocities can be calculated from the corresponding hopping amplitudes (γ_i) using the conversion rule $v_i = \sqrt{3}|\gamma_i|a/(2\hbar)$ with $a = 2.46 \text{ \AA}$. For our calculations, we consider the following parameters: the dimer site potential $\delta = 15 \text{ meV}$, the intra-layer hopping $\gamma_0 = -3.1 \text{ eV}$, which gives the Fermi velocity, $v_F = 10^6 \text{ m/s}$ and $\gamma_1 = 361 \text{ meV}$. The remote hopping amplitudes γ_3 and γ_4 are considered to be 283 meV and 138 meV , respectively.

The moiré coupling between the twisted bilayers (coupling between the two adjacent rotated layers) in Eq. (S1) can be expressed as, $T(\mathbf{r}) = \sum_{j=b,tl,tr} T_{\mathbf{q}_j} e^{-i\mathbf{q}_j \cdot \mathbf{r}}$. The hopping paths are given by the three vectors $\mathbf{q}_b = \frac{8\pi}{3a} \sin \frac{\theta}{2} (0, -1)$, $\mathbf{q}_{tr} = \frac{8\pi}{3a} \sin \frac{\theta}{2} (\frac{\sqrt{3}}{2}, \frac{1}{2})$ and $\mathbf{q}_{tl} = \frac{8\pi}{3a} \sin \frac{\theta}{2} (-\frac{\sqrt{3}}{2}, 1/2)$ and the hopping matrices are given by,

$$T_b = \begin{pmatrix} \omega' & \omega \\ \omega & \omega' \end{pmatrix}; \quad T_{tr,tl} = \begin{pmatrix} \omega' & \omega e^{\mp i2\pi/3} \\ \omega e^{\mp i2\pi/3} & \omega' \end{pmatrix}. \quad (\text{S2})$$

The diagonal (ω') and off-diagonal (ω) hopping strengths have been considered to be unequal due to the out-of-plane corrugation effect and chosen in the scale 79 meV and 106 meV , respectively. The tunability of the electronic band structure of the TDBG due to perpendicular electric field is included in the model Hamiltonian by means of inter-layer potential difference parameter Δ . To model the effective electric field as a constant gradient in potential, we use $\Delta_b^- = -\Delta_t^+ = \frac{3}{2}\Delta$ and $\Delta_t^- = -\Delta_b^+ = \frac{1}{2}\Delta$.



Supplementary Fig. S1. **a**, The side view of the Bernal stacked (AB-stacked) bilayer graphene. The hopping paths corresponding to γ_1 , γ_3 and γ_4 are shown by black solid, dashed and dotted lines. **b**, Schematic of hexagonal moiré BZ. Three nearest neighbor connecting vectors, \mathbf{q}_b , \mathbf{q}_{lr} and \mathbf{q}_{ll} are shown by red, blue and green arrows respectively. The high symmetry points in the moiré BZ are indicated by K, Γ , M and K' along which we plot the band dispersion (shown by cyan dashed line). **c**, The Berry curvature (in units of \AA^2) distribution in the moiré BZ for conduction (left) and valence (right) bands in presence of $\epsilon = 0.1\%$ strain. The k_x and k_y axes are normalized with $k_\theta = 8\pi/(3a)\sin(\theta/2)$ with $a = 2.46 \text{ \AA}$. **d**, The distribution of the Berry curvature dipole integrand of Eq. (S5) $[\frac{\partial \epsilon}{\partial k_y} \Omega_z]$ over the Fermi surface in units of $\text{meV} \cdot \text{\AA}^3$, in the isolated conduction flat band, without strain (left panel) and with strain (right panel) applied along the zigzag edge of graphene.

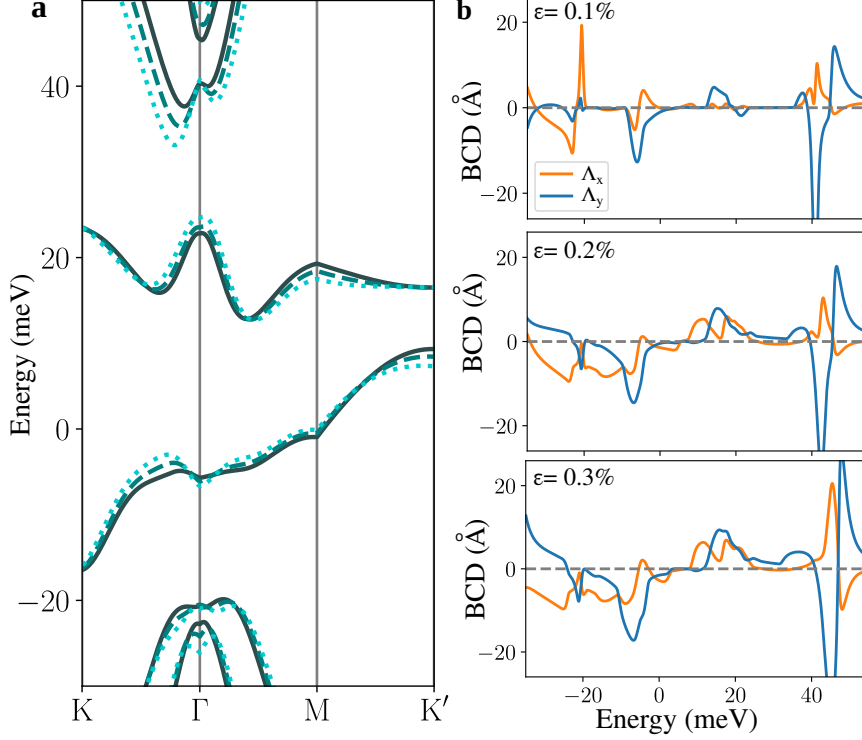
II Impact of strain on electronic structure of TDBG

Equation (S1) and the corresponding band structure explain the measured resistance as a function of charge density and displacement field reasonably well. However, it can not account for the measured nonlinear Hall voltage due to the presence of C_3 symmetry in the continuum model. So to break the C_3 symmetry we include the effect of uniaxial strain quantified as [3]

$$\mathcal{E} = \epsilon \begin{pmatrix} -\cos^2 \phi + \nu \sin^2 \phi & -(1 + \nu) \sin \phi \cos \phi \\ -(1 + \nu) \sin \phi \cos \phi & -\sin^2 \phi + \nu \cos^2 \phi \end{pmatrix}, \quad (\text{S3})$$

which breaks the C_3 symmetry [2, 3, 15, 30]. In Eq. (S3) ϵ is the strength of strain, ν is the Poisson ratio (~ 0.16 for graphene) and ϕ is the strain angle with respect to zigzag direction of graphene. The strain matrix has two fold impact on the model Hamiltonian—i) The Dirac points of bilayer gets shifted to $\mathbf{D} = (1 - \mathcal{E}^T)\mathbf{K} - \mathbf{A}$ from \mathbf{K} with $\mathbf{A} = \frac{\beta}{d}(\epsilon_{xx} - \epsilon_{yy}, -2\epsilon_{xy})$ (where $\beta = 1.57$ and $d = 1.42 \text{ \AA}$) being the strain induced effective gauge field. As a result the moiré coupling vectors and the hopping matrices get modified. ii) The Dirac Hamiltonian itself modifies to $\hbar v_F \tilde{R}_{\frac{\theta}{2}} [(1 + \mathcal{E}^T)\mathbf{k} \cdot \boldsymbol{\sigma}]$. In our calculation we extend the strain implementation of Ref. [3] for twisted bilayer graphene to the TDBG where the hetero strain is applied solely on the lower bilayer.

The breaking of C_3 symmetry after strain implementation in the Hamiltonian is highlighted in Fig. 1b, c of the main manuscript where the Berry curvature (Ω) of the valence band is plotted along three paths arranged in 120° angle as shown by the blue, orange and green arrows in Fig. 1a of the main manuscript. The Berry curvature is calculated using the periodic part of the Bloch



Supplementary Fig. S2. **a**, Solid, dashed and dotted lines represent band structure with $\epsilon = 0.1\%$, 0.2% and 0.3% strain respectively for $\Delta = 11$ meV. **b**, In top, middle and bottom panel, the x and y components of Berry curvature dipole are shown for strain strength $\epsilon = 0.1\%$, 0.2% and 0.3% , respectively.

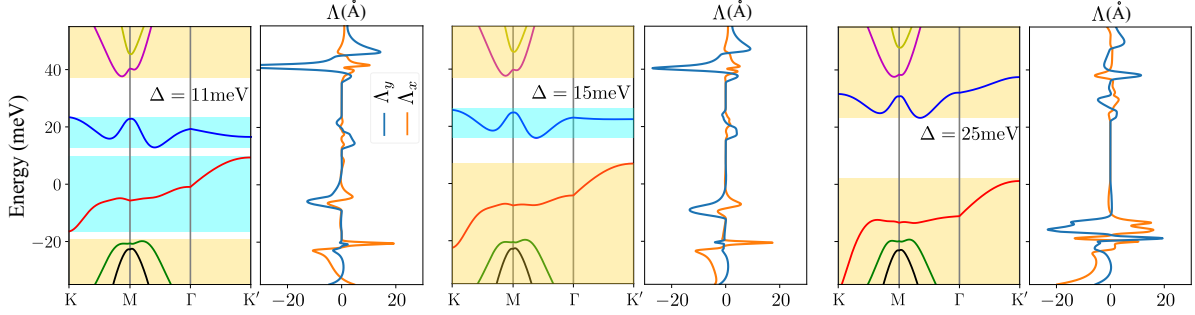
wave-function, $H|u_n\rangle = E_n|u_n\rangle$, as

$$\Omega^n \equiv \Omega_z^n = -2\text{Im} \sum_{m \neq n} \frac{\langle u_n | \partial_{k_x} H | u_m \rangle \langle u_m | \partial_{k_y} H | u_n \rangle}{(E_n - E_m)^2}. \quad (\text{S4})$$

In Supplementary Fig. S1c we have shown the Berry curvature distribution for the conduction (left column) and valence (right column) bands over the moiré BZ. Due to the broken C_3 symmetry, the distribution of Berry curvature in the \mathbf{k} -space becomes non-symmetric. Such non-symmetric Berry curvature in the moiré Brillouin zone (mBZ) recently has been shown to cause nonlinear Hall effect which is quantified by Berry curvature dipole (BCD) defined as

$$D_{cd} = \sum_{n, \xi, g_s} \int_{\text{mBZ}} \frac{d\mathbf{k}}{(2\pi)^2} \Omega_d^n \frac{\partial \epsilon_{\mathbf{k}}^n}{\hbar \partial k_c} \frac{\partial f(\epsilon_{\mathbf{k}}^n)}{\partial \epsilon_{\mathbf{k}}^n}. \quad (\text{S5})$$

Here, n is the band index, ξ is the valley index, g_s is the spin index and f_0 is the Fermi-Dirac distribution function. For a two dimensional system (TDBG in our case) the Berry curvature acts as pseudo-scalar and has only z -component. So depending on the direction of velocity, $\frac{\partial \epsilon^n}{\partial k_c}$, the BCD has only two components $D_{xz} \equiv \Lambda_x \equiv \text{BCD}_x$ and $D_{yz} \equiv \Lambda_y \equiv \text{BCD}_y$. The distribution of the Berry curvature dipole kernel, $\frac{\partial \epsilon}{\partial k_y} \Omega_z$ of the flat conduction band is highlighted in Supplementary Fig. S1d where the left panel shows the kernel in absence of strain and the right panel shows the kernel in presence of 0.1% strain. The variation of BCD with the strain strength is shown in Supplementary Fig. S2 where three different magnitude of strain: 0.1% , 0.2% and 0.3% are considered.



Supplementary Fig. S3. The evolution of band structure and Berry curvature dipole in presence of 0.1% strain for three different Δ values: $\Delta = 11, 15$ and 25 meV. The left most panel shows the BCD when CNP gap as well as both the moiré gaps are present. The middle one highlights the scenario when the valence band side moiré gap is closed. The right most panel reveals the BCD when only the CNP gap is present.

III Variation of band structure and Berry curvature dipole with electric field in presence of strain

One of the experimental advantages of TDBG in comparison to the TBG counterpart is that one can tune the electronic band dispersion and hence related physical properties by an external electric field. This electric field tunability is captured in our Hamiltonian, Eq. S1, by the Δ term. In this section, we discuss how the band structure and Berry curvature dipole evolve with the variation in external electric field in presence of strain. This is shown in Supplementary Fig. S3 (with 0.1% strain) and we find that the evolution of the band structure is qualitatively consistent with our experimental findings. In absence of an external electric field, i.e. $\Delta = 0$ meV, the strained flat bands overlap and promote a metallic state. At the same time the flat bands are separated from the higher moiré bands by a finite energy gap, namely moiré gap.

Application of finite external electric field pushes the flat bands away from each other. However, a gap at charge neutrality point (CNP) appears only after certain threshold electric field and in our model calculations we find it to be ~ 9.5 meV. At $\Delta = 11$ meV, the CNP gap as well as both the moiré gaps exist simultaneously. The corresponding band structure and BCD are shown in the left most column of Supplementary Fig. S3. Gradual increment of Δ enhances the CNP gap and decreases the magnitude of both the moiré gaps. At $\Delta \sim 13$ meV the valence flat band merges with higher moiré bands while the conduction moiré gap remains finite. This scenario of band structure and corresponding BCD are indicated in the middle column of Supplementary Fig. S3. Further increment in Δ eventually closes the moiré gap at conduction band side and only the CNP gap persists. The right most column of Supplementary Fig. S3 shows the band structure and BCD at $\Delta = 25$ meV.

IV Sign reversal of Berry curvature dipole across the topological phase transition

The electronic wave-functions in TDBG are known to be rich in topological aspects. It has been predicted that tuning the strength of the electric field or twist angle can give rise to a topological phase-transition in this system. However, to the best of our knowledge, topological phase transition in TBG/TDBG has not been experimentally demonstrated. In our experiment we observe a topological phase-transition by tuning the electric field, which manifests as the sign reversal of BCD.

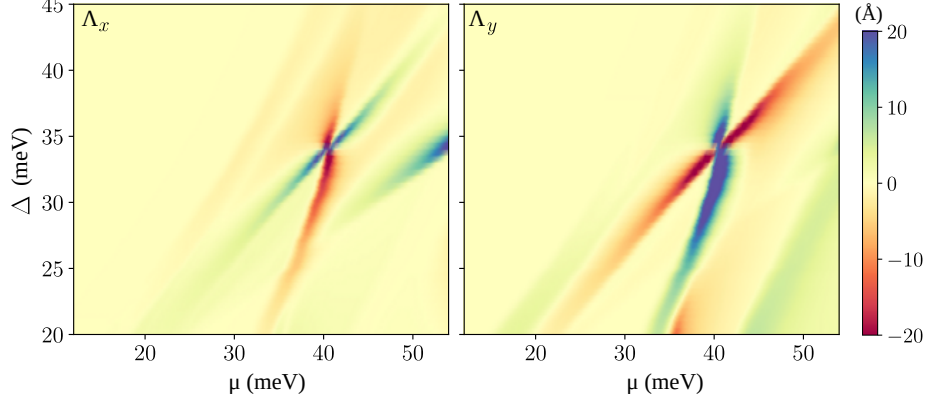
The non-trivial topology of the electronic wave-functions in TDBG is characterized by the valley Chern number (C_v) [9]. For an isolated band, the Chern number in each valley can be calculated by integrating the Berry curvature in the mBZ as

$$C_v^n = \frac{1}{2\pi} \int_{\text{mBZ}} d\mathbf{k} \Omega^n. \quad (\text{S6})$$

Due to the presence of time reversal symmetry, the Chern numbers for K and K' valley are equal and opposite which makes the total (adding the two valleys) Chern number, for a particular band, zero. So to distinguish different topological phases we define a topological invariant (Z) as $Z = |(C_K - C_{K'})/2|$, where C_K and $C_{K'}$ are the Chern numbers for K and K' valley, respectively. A topological phase transition is identified with a change in the associated Z index, ΔZ . In presence of $\epsilon = 0.1$ % strain we find a topological phase-transition near $\Delta \sim 34$ meV in our calculation. We emphasize that both the phases across the topological transition are robust in a large window of Δ .

The band dispersion, Chern number and Berry curvature dipole in these two distinct topological phases are shown in Fig. 3e-h of the main manuscript. The bands plotted in Fig. 3f indicate the phase before the transition ($\Delta = 25$ meV) for the K valley. The corresponding Chern numbers of the first conduction and first valence bands are 2 and -2, respectively resulting in $Z= 2$ for both the bands. For $\Delta = 38$ meV, the band dispersion after the phase-transition, is plotted in Fig. 3e. The calculated Chern numbers for this phase are 0 and 1 for the first conduction and first valence bands, respectively. This results in $Z= 0$ for the first conduction band and $Z= 1$ for the first valence band. Therefore the phase transition in conduction band is conveyed through $\Delta Z = 2$ and in the valence band through $\Delta Z = 1$. Note that some recent literature reports the Chern numbers of the flat bands can be tunable upto ± 3 with variation in twist angle and electric field for the unstrained moiré systems [3–5]. Interestingly the phase-transition near $\Delta = 34$ meV is also evident from the band structure evolution across the critical point. Focusing on the conduction band side, we find that as we gradually increase the electric field from $\Delta = 25$ meV, the first conduction band gets closer to the higher conduction bands. However, it starts to move away from the higher band as we cross the critical point. Remarkably, we find that the BCD changes its sign across this phase transition which is also highlighted in Fig. 3g, h of the main manuscript. The similar BCD peaks for two different phases are shown with arrows of same color. We emphasize here the exact values of Chern numbers crucially depends on the chosen parameters. However, the topological transition which is associated with finite value of ΔZ for each flat band can be seen for a broad range of parameters.

To emphasize the topological phase-transition more comprehensively we have plotted the x - and y -components of BCD as a function of perpendicular electric field (Δ) and chemical potential (μ) in Supplementary Fig. S4 in presence of 0.1% strain along zigzag direction ($\phi = 0$). A clear sign of perpendicular electric field induced phase-transition can be realized from the butterfly like structure near $\Delta = 34$ meV. Before the phase-transition ($\Delta < 34$ meV) the x -component of BCD of the first conduction band has positive sign (shown by the blue lobe) and the second conduction band has negative sign (shown by the red lobe). However, after the phase-transition this trend gets reversed as the first conduction band possesses negative BCD_x (shown by the red lobe) and the second conduction band possesses positive BCD_x (shown by the blue lobe). Apart from the fact that the sign of the y -components of the BCD is opposite to the corresponding x -component, BCD_y also shows a similar behavior. This abrupt change in the sign of BCD near $\Delta \sim 34$ meV indicates a topological transition. We emphasize here that we have considered $\mu = 0$ to reside in the maxima of the valence band and the shaded region near $\mu \sim 50$ meV is contribution of the further higher conduction bands to the BCD.



Supplementary Fig. S4. Dependence of the Berry curvature dipole on the chemical potential (μ) and perpendicular electric field (Δ) at the conduction band side. The butterfly like structure near $\Delta = 34$ meV indicates a perpendicular electric field induced topological phase-transition.

V Origin of BCD in graphene based moiré materials

In this section we explore the origin of large BCD in graphene based moiré systems, in vicinity of the charge neutrality point. For that we calculate Berry curvature dipole for a low energy tilted massive Dirac model and extend it to strained two band model of twisted bilayer graphene [40]. The nonlinear Hall conductivity for a tilted massive Dirac Hamiltonian of the form

$$\mathcal{H} = \hbar t k_x \sigma_0 + \hbar v k_x \sigma_x + \hbar v k_y \sigma_y + m \sigma_z \quad (\text{S7})$$

can be written as $\sigma_{yxx} = \frac{e^3 \tau}{\hbar} \text{BCD}_x$ in the limit $\omega \tau \ll 1$, which is valid for transport experiments. Up to linear order in the tilt value, the x -component of the BCD at chemical potential μ is given by

$$\text{BCD}_x = \frac{3m\hbar t}{8\pi\mu^2} \left(1 - \frac{m^2}{\mu^2} \right). \quad (\text{S8})$$

From this expression we infer that within the constant scattering time approximation the BCD is proportional to the tilt and the BCD peak in μ -axis is determined by the tilt and Berry curvature hotspot.

The low energy mode for strained twisted bilayer graphene given, in vicinity of the charge neutrality point, is given by [40]

$$\mathcal{H} = -\frac{\hbar}{1+6\alpha^2} \psi_0^\dagger \left[v_{0x} k_x + v_{0y} k_y + \xi \sigma_x v_x k_x + \sigma_y v_y k_y + \xi \sigma_x v_{xy} k_y + \sigma_y v_{yx} k_x + m \sigma_z \right] \psi_0. \quad (\text{S9})$$

Here, $\alpha = w/(\hbar v_F k_\theta)$ with $k_\theta = 8\pi/(3a) \sin(\theta/2)$ and the various velocities are modified by strain as shown in Ref. [40]. In Eq. (S9) while v_{0x}, v_x, v_y are determined by the off-diagonal components of strain matrix, the other components v_{0y}, v_{xy}, v_{yx} are determined by the diagonal components of strain matrix [40]. For a rough estimation, we will consider shear strain (diagonal components of strain are zero) where the tilt velocity is given by

$$v_{0x} = -\xi v_F \frac{\alpha^2}{1+6\alpha^2} \frac{16\pi}{ak_\theta} \epsilon_{xy}. \quad (\text{S10})$$

Using this tilt value in Eq. (S8), we have

$$\text{BCD}_x \propto t \propto v_{0x} \propto k_\theta^{-3} \epsilon_{xy}. \quad (\text{S11})$$

This simple estimate indicates that the BCD is larger for systems with i) large moiré lengthscale, and ii) with a large strain.

VI Scaling of nonlinear Hall Effect

In this section we describe the scaling law of the experimentally measured quantity $\frac{V_y^N}{(V_x^L)^2}$ which is related to the theoretically calculated nonlinear Hall conductivity σ_{yxx} and Drude conductivity σ_{xx} as

$$\frac{V_y^N}{(V_x^L)^2} = \frac{\sigma_{yxx}}{\sigma_{xx}}. \quad (\text{S12})$$

The non-linear Hall conductivity can originate from three different sources: i) the Berry curvature dipole, ii) side-jump scattering and iii) skew-scattering (also called anti-symmetric scattering). For a tilted massive Dirac model Hamiltonian it can be shown that [39] the Berry curvature dipole and the side-jump contributions to σ_{yxx} are inversely proportional to the impurity concentration making the ratio in Eq. (S12) to be scattering independent. However, the skew-scattering part has different impurity concentration dependence. Accounting for all the terms, we can write a general scaling relation, following Du et al. [39],

$$\frac{V_y^N}{(V_x^L)^2} = \mathcal{C}^{in} + \sum_i \mathcal{C}_i^{sj} \frac{\rho_i}{\rho_{xx}} + \sum_{i,j} \mathcal{C}_{ij}^{sk1} \frac{\rho_i \rho_j}{\rho_{xx}^2} + \sum_i \mathcal{C}_i^{sk2} \frac{\rho_i}{\rho_{xx}^2}. \quad (\text{S13})$$

Here, i, j represent different source of scattering, the superscripts in , sj and sk stands for Berry curvature dipole, side-jump and skew-scattering contributions respectively. Considering only two sources of scattering, the static (impurities) and dynamic (phonon), we can write the above equation as follows

$$\frac{V_y^N}{(V_x^L)^2} = \frac{1}{\rho_{xx}^2} (\mathcal{C}_1 \rho_{xx0} + \mathcal{C}_2 \rho_{xx0}^2 + \mathcal{C}_3 \rho_{xx0} \rho_{xxT} + \mathcal{C}_4 \rho_{xxT}^2). \quad (\text{S14})$$

Here, ρ_{xx0} is the residual resistivity and $\rho_{xxT} = \rho_{xx} - \rho_{xx0}$ is the dynamical resistivity. The new parameter set in Eq. (S14) can be obtained from the old one as

$$\mathcal{C}_1 = \mathcal{C}_0^{sk2}; \mathcal{C}_2 = \mathcal{C}^{in} + \mathcal{C}_0^{sj} + \mathcal{C}_{00}^{sk1}, \quad (\text{S15})$$

$$\mathcal{C}_3 = 2\mathcal{C}^{in} + \mathcal{C}_0^{sj} + \mathcal{C}_1^{sj} + \mathcal{C}_{01}^{sk2}, \quad (\text{S16})$$

$$\mathcal{C}_4 = \mathcal{C}^{in} + \mathcal{C}_1^{sj} + \mathcal{C}_{11}^{sk1}. \quad (\text{S17})$$

For finite temperature, using $\rho_{xxT} = \rho_{xx} - \rho_{xx0}$, we can write the scaling law in terms of the conductivities as

$$\begin{aligned} \frac{V_y^N}{(V_x^L)^2} - \mathcal{C}_1 \sigma_{xx0}^{-1} \sigma_{xx}^2 &= (\mathcal{C}_2 + \mathcal{C}_4 - \mathcal{C}_3) \sigma_{xx0}^{-2} \sigma_{xx}^2 \\ &+ (\mathcal{C}_3 - 2\mathcal{C}_4) \sigma_{xx0}^{-1} \sigma_{xx} + \mathcal{C}_4. \end{aligned} \quad (\text{S18})$$

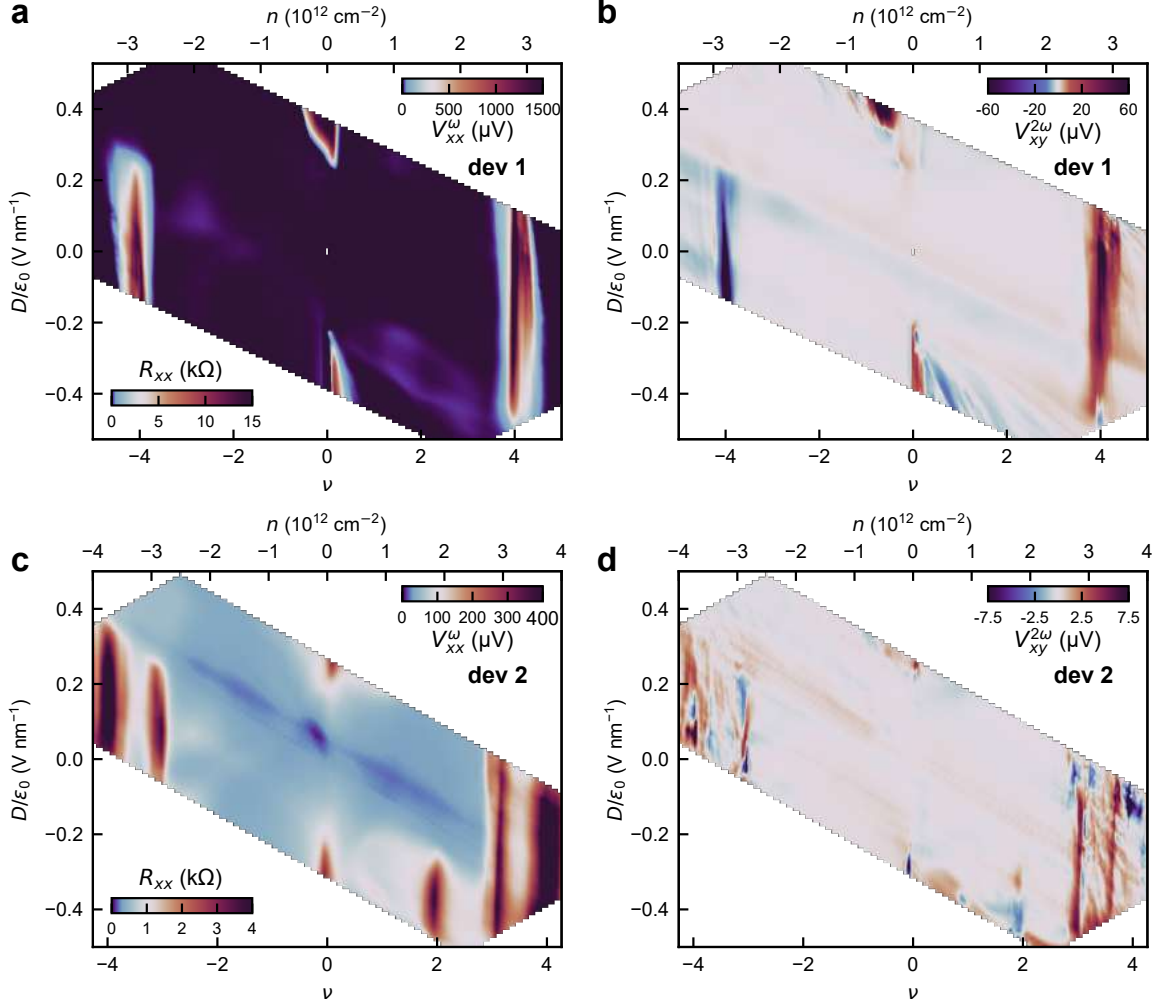
For experimental fitting we use a more simplified scaling law which reads as

$$\frac{V_y^N}{(V_x^L)^2} = A \sigma_{xx}^2 + B, \quad (\text{S19})$$

where A represents the slope and B is the intercept. From Eq. (S18) it is evident that the slope A does not include any Berry curvature dipole contribution and is solely determined by the skew-scattering and side-jump mechanism. The intercept B contains information of BCD.

VII NLH voltage from other TDBG devices

In Supplementary Fig. S5a and Supplementary Fig. S5b, we show the dependence of longitudinal resistance and nonlinear Hall voltage, respectively, on filling factor ν and displacement field D/ϵ_0 . The data is taken from device-1 presented in main manuscript having a twist angle of 1.1° , using a different set of probes. Supplementary Fig. S5c and Supplementary Fig. S5d shows the dependence of longitudinal resistance and nonlinear Hall voltage, respectively, on ν and D/ϵ_0 from a different TDBG device (device-2) with a twist angle of 1.26° . The additional vertical feature of high resistance in Supplementary Fig. S5c close to $n = 2.9 \times 10^{12} \text{ cm}^{-2}$ can be attributed to moiré gap from a regime in device-2 having a slightly different twist angle of 1.09° . Twist angle variation in same device is a signature of strain that breaks C_3 symmetry and give rise to BCD. In all the cases, the characteristic cross and halo feature that is present in the longitudinal resistance color plots (in Supplementary Fig. S5a, Supplementary Fig. S5c herein and also in Fig. 2a of main manuscript) is absent in the NLH voltage color plots (in Supplementary Fig. S5b, Supplementary Fig S5d herein and also in Fig. 2b of main manuscript). This shows the universality of NLH voltage across multiple TDBG devices and that the NLH signal only persists close to either the CNP or the moiré gaps, as discussed in the main manuscript.



Supplementary Fig. S5. NLH voltage in other TDBGs. **a, b**, Longitudinal voltage (V_{xx}^{ω}) (**a**) and nonlinear Hall voltage ($V_{xy}^{2\omega}$) (**b**) as a function of filling factor (ν) and perpendicular electric displacement field (D/ϵ_0) at a temperature of 1.5 K. The voltages are measured using a different set of probes than that in main manuscript for the 1.1° device. **c, d**, Longitudinal voltage (V_{xx}^{ω}) (**c**) and Nonlinear Hall voltage ($V_{xy}^{2\omega}$) (**d**) as a function of ν and D/ϵ_0 at a temperature of 10 mK for another TDBG device with a twist angle of 1.26° . The top x-axis indicates the charge density (n). The color bar provided in bottom left of **a** and **c** indicates the corresponding values of the longitudinal resistance (R_{xx}) measured using 4-probe method. All the measurements are performed using a constant current $I = 100$ nA sent with frequency $\omega = 177$ Hz.

VIII Characterization of NLH voltage

VIII.1 Quadratic nature

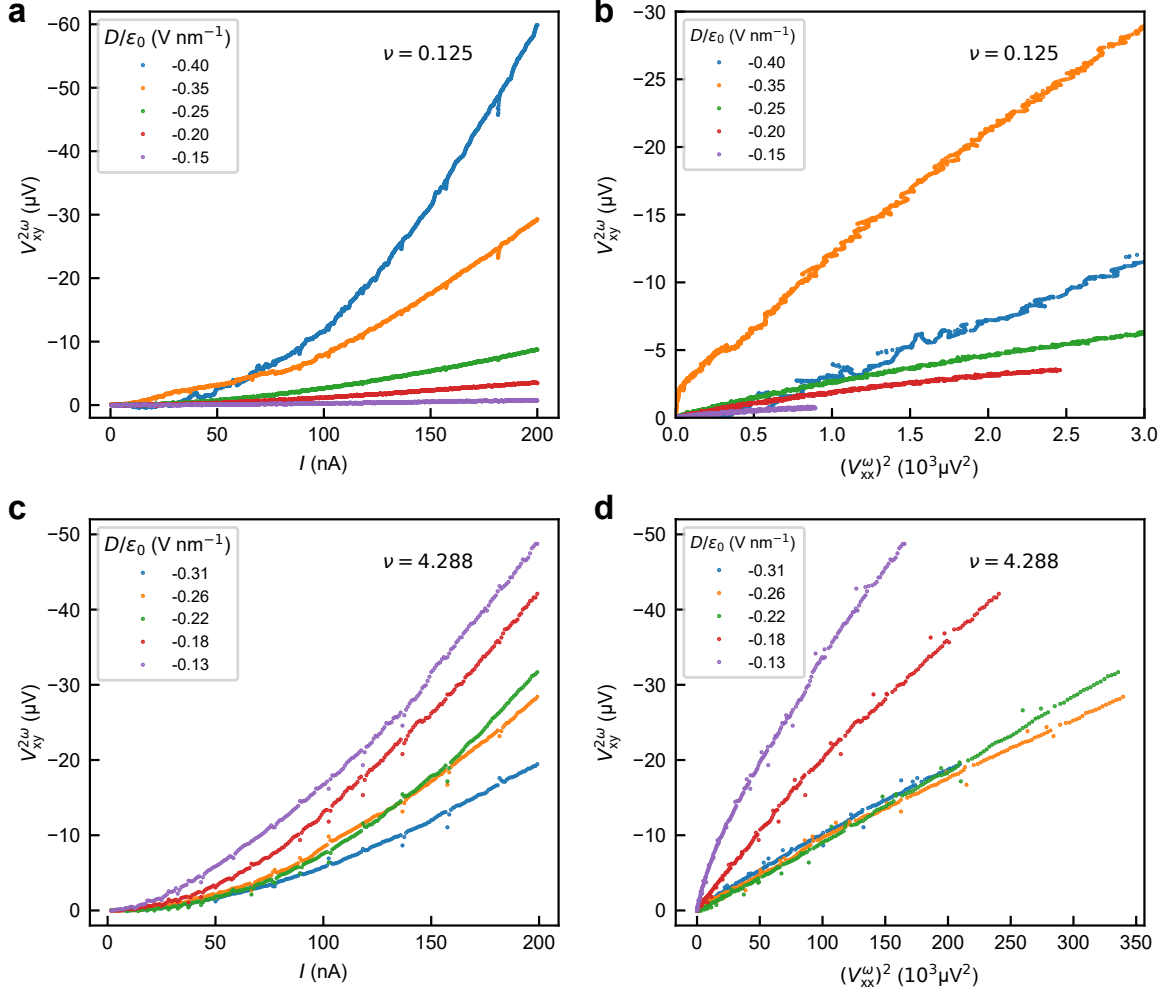
In Supplementary Fig. S6a, we show the quadratic scaling of the NLH voltage ($V_{xy}^{2\omega}$) with current for the same filling $\nu = 0.125$ used in Fig. 3a and 3b of main manuscript. In Fig. S6b shows the linear dependence of $V_{xy}^{2\omega}$ on square of the longitudinal voltage (V_{xx}^ω). A linear behavior establishes quadratic scaling of NLH voltage, that we measure, with current. Supplementary Fig. S6a and Supplementary Fig. S6b together shows that the quadratic nature persists in the regime of displacement field we use to extract BCD in Fig 3b of main manuscript. Supplementary Fig. S6c shows the quadratic scaling of the NLH voltage that corresponds to a filling $\nu = 4.288$ close to the electron-side moiré gap. We see departure from linear behavior in Supplementary Fig. S6d for few displacement fields towards high values of V_{xx}^ω . This is outside the scope of our present study.

VIII.2 Phase

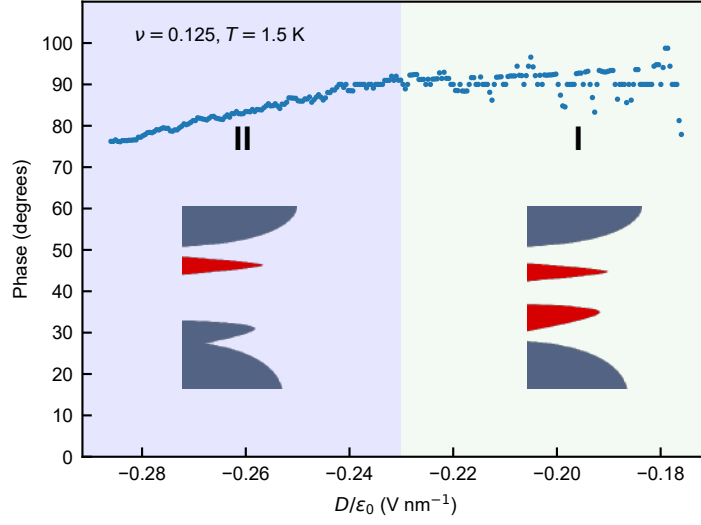
In Supplementary Fig. S7, we show the phase of the measured NLH voltage as a function of displacement field for the filling $\nu = 0.125$. The filling and the range of displacement field is same to that we explore in Fig. 3a and 3b of main manuscript. When an ac current $I = I_0 \sin \omega t$ is sent, quadratic scaling of the second harmonic NLH voltage dictates that $V_{xy}^{2\omega} \propto I^2 \propto I_0^2 \sin^2 \omega t = I_0^2 (1 + \sin(2\omega t - \pi/2))/2$. The phase remains close to 90° across the two regimes, which is consistent to the second order nature of $V_{xy}^{2\omega}$. We additionally note that we measured the out-of-phase component of the NLH voltage consistently throughout all the data presented in main manuscript and supplementary.

VIII.3 NLH voltage at other frequency

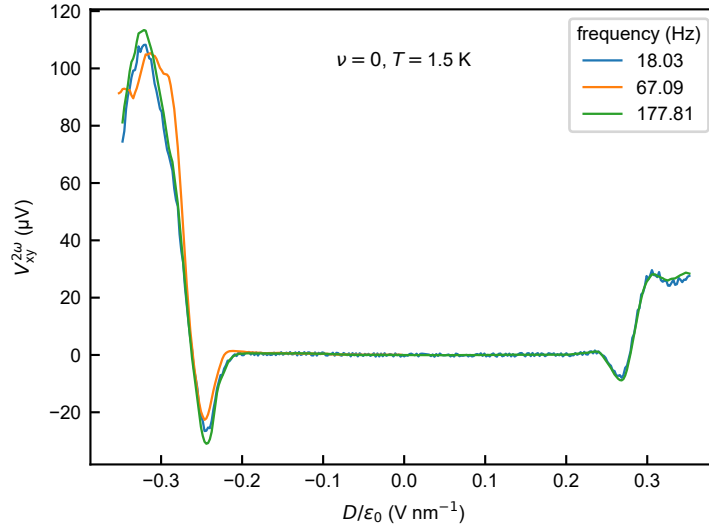
Supplementary Fig. S8 shows the nonlinear Hall voltage ($V_{xy}^{2\omega}$) dependence on displacement field for three different frequencies of the driving current. No frequency dependence of $V_{xy}^{2\omega}$ is observed even when the frequency we explored is varied by an order of magnitude (from ~ 18 -178 Hz). This is consistent to earlier reports [17, 18, 23]. Theoretically, independence of NLH voltage with frequency in the low-frequency regime such that $\omega\tau \rightarrow 0$, where ω is the frequency and τ is the scattering time, is a signature that the NLH voltage is BCD-induced [11].



Supplementary Fig. S6. Additional quadratic scaling data. **a, b,** Quadratic dependence of $V_{xy}^{2\omega}$ on current (I) (**a**) and linear dependence of $V_{xy}^{2\omega}$ on $(V_{xx}^\omega)^2$ (**b**) for the same filling $\nu = 0.125$ as in Fig. 3b of main manuscript, at different displacement fields. **c, d,** Quadratic dependence of $V_{xy}^{2\omega}$ on current (I) (**c**) and linear dependence of $V_{xy}^{2\omega}$ on $(V_{xx}^\omega)^2$ (**d**) for a filling close to electron-side moiré gap at $\nu = 4.288$, for different displacement fields.



Supplementary Fig. S7. Phase of nonlinear Hall voltage. Variation of the phase of the nonlinear Hall voltage with displacement field for the same filling $\nu = 0.125$ and temperature $T = 1.5$ K as in Fig. 3b of main manuscript. The cartoon indicates the density of states in the two regimes I (light green background) and II (light blue background).



Supplementary Fig. S8. Frequency dependence of nonlinear Hall voltage. The nonlinear Hall voltage $V_{xy}^{2\omega}$ vs. displacement field, measured at a frequency of 2ω for current with three different frequencies, $\omega = 18.03$ Hz (blue line), 67.09 Hz (orange line) and 177.81 Hz (green line). $V_{xy}^{2\omega}$ remains constant even when the frequency (ω) of current is varied by an order of magnitude. The data is taken for a fixed filling $\nu = 0$ and temperature $T = 1.5$ K. The data corresponding to orange curve was taken for $D < 0$.

IX Scaling of NLH voltage with conductivity

IX.1 $V_{xy}^{2\omega}/(V_{xx}^\omega)^2$ vs σ_{xx}^2 using displacement field as parameter for different fixed temperature

In Supplementary Fig. S9a, we show the dependence of $V_{xy}^{2\omega}/(V_{xx}^\omega)^2$ on (σ_{xx}^2) using D/ϵ_0 as a parameter for the same filling $\nu = 0.125$ where the range of $|D|/\epsilon_0$ extends below 0.175 V/nm (in Fig. 3b of main manuscript, $|D|/\epsilon_0$ is varied till 0.175 V/nm). We see that at lower displacement fields, $V_{xy}^{2\omega}/(V_{xx}^\omega)^2$ is close to zero. Interestingly, from Extended Data Fig. 3b, we note that as the magnitude of displacement field is decreased to below 0.18 V/nm, the R vs T at $\nu = 0$ becomes metallic, indicating a closing of the gap between the flat bands. Supplementary Fig. S9b shows $V_{xy}^{2\omega}/(V_{xx}^\omega)^2$ dependence on σ_{xx}^2 at an elevated temperature of $T = 12$ K for the same filling $\nu = 0.125$. Here, we see that the intercept is very close to zero in regime-I as well, that was otherwise nonzero at $T = 1.5$ K in Supplementary Fig. S9a. The inset in Supplementary Fig. S9b shows the variation of the y-intercept in regime-I, as a function of temperature. Systematic variation of the intercept (or, $V_{xy}^{2\omega}/(V_{xx}^\omega)^2$ for $\sigma \rightarrow 0$) with T confirms additionally that $V_{xy}^{2\omega}/(V_{xx}^\omega)^2$ for $\sigma \rightarrow 0$, as we extract in Fig. 3d of main manuscript, is related to BCD.

IX.2 Extracting BCD via a second method

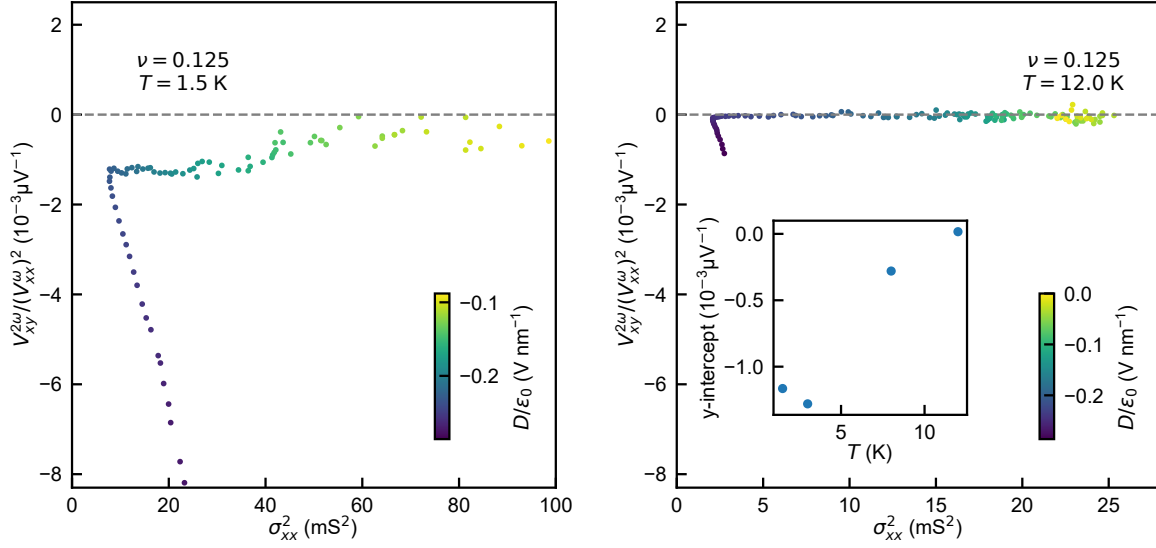
For low frequency, the BCD (Λ) can also be represented as [11, 18]

$$\Lambda = \frac{2\hbar^2 \sigma_{xx}^3 V_{xy}^{2\omega} W}{e^3 \tau I^2}. \quad (\text{S20})$$

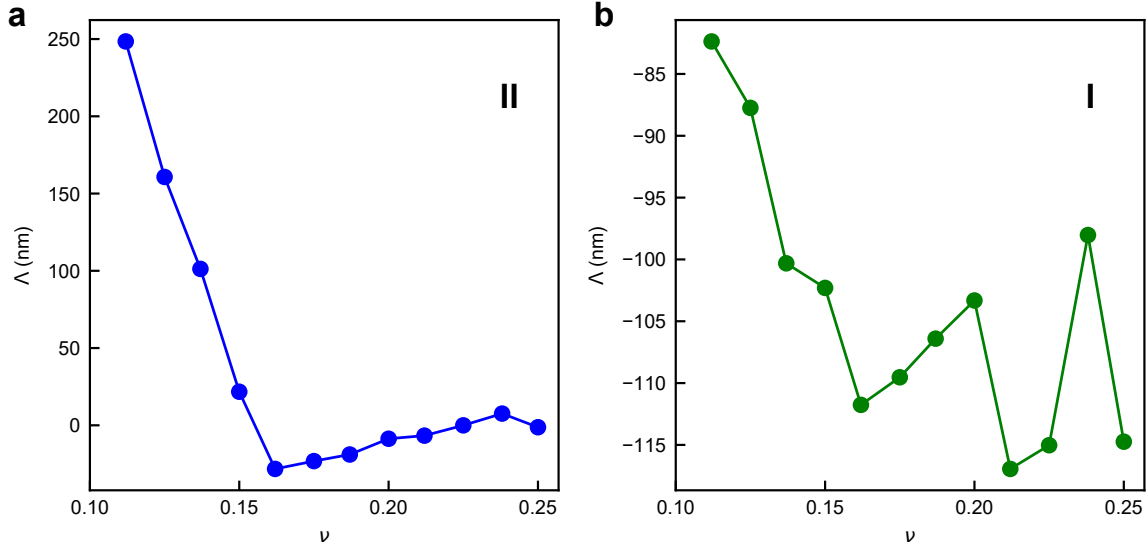
Here, σ_{xx} is the longitudinal conductivity, $V_{xy}^{2\omega}$ is the nonlinear Hall voltage, W is the width of TDBG, τ is the scattering time, I is the current sent with low frequency and e is the electronic charge. Using Drude formula, $\sigma_{xx} = ne^2\tau/m$, where n is the charge density and m is the effective mass, and $\sigma_{xx} = \frac{IL}{V_{xx}^\omega W} = \frac{I}{V_{xx}^\omega}$ (for our case, length (L)=width (W)= $2 \mu m$) in eq. (S20), we obtain

$$\Lambda = \frac{2\hbar^2 W n}{em} \times \left(\frac{V_{xy}^{2\omega}}{(V_{xx}^\omega)^2} \right). \quad (\text{S21})$$

In Supplementary Fig. S10, we plot the BCD using eq. (S21) using $\frac{V_{xy}^{2\omega}}{(V_{xx}^\omega)^2}$ for $\sigma_{xx} \rightarrow 0$ (the y-intercept in Fig. 3b of main manuscript) for different fillings $\nu = 4n/n_S$. Here, $n_S = 2.8 \times 10^{12} \text{ cm}^{-2}$ is the required charge density to completely fill the flat conduction band, corresponding to a twist angle of 1.1° . With an assumption of $m=3m_e$, where m_e is mass of electron, we get a good agreement with the BCD extracted in Fig. 3c of main manuscript.



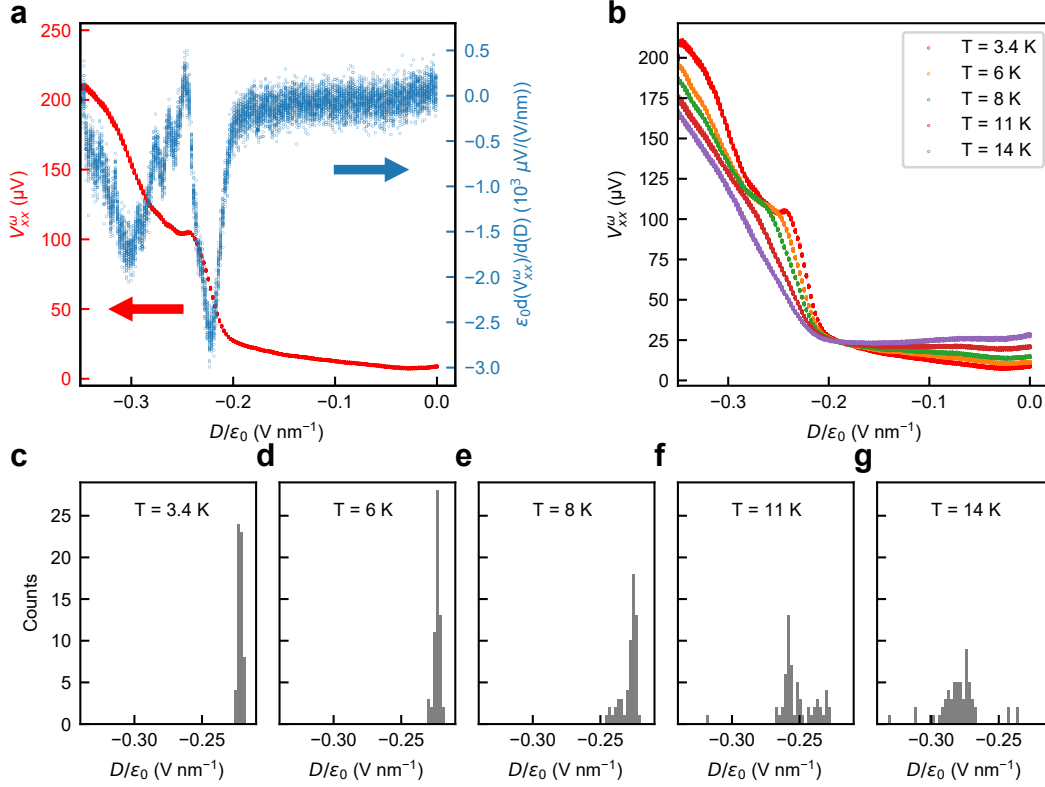
Supplementary Fig. S9. Scaling of $V_{xy}^{2\omega}/(V_{xx}^\omega)^2$ vs σ_{xx}^2 at elevated temperatures. **a, b**, The variation of normalized nonlinear Hall voltage $V_{xy}^{2\omega}/(V_{xx}^\omega)^2$ with square of longitudinal conductivity σ_{xx}^2 plotted parametrically as a function of the displacement field D/ϵ_0 for $T = 1.5$ K (**a**) and $T = 12$ K (**b**) at $\nu = 0.125$. The color of the data points indicate the corresponding displacement field. The horizontal dashed gray line at $V_{xy}^{2\omega}/(V_{xx}^\omega)^2 = 0$ is a guide to the eye. The inset in **b** shows the extracted y-intercept of the normalized nonlinear Hall voltage $V_{xy}^{2\omega}/(V_{xx}^\omega)^2$ for regime-I at few other temperatures for the same filling.



Supplementary Fig. S10. a, b, Extracting the BCD as a function of filling (ν) using eq. (S21) for regime-II (**a**) and regime-I (**b**).

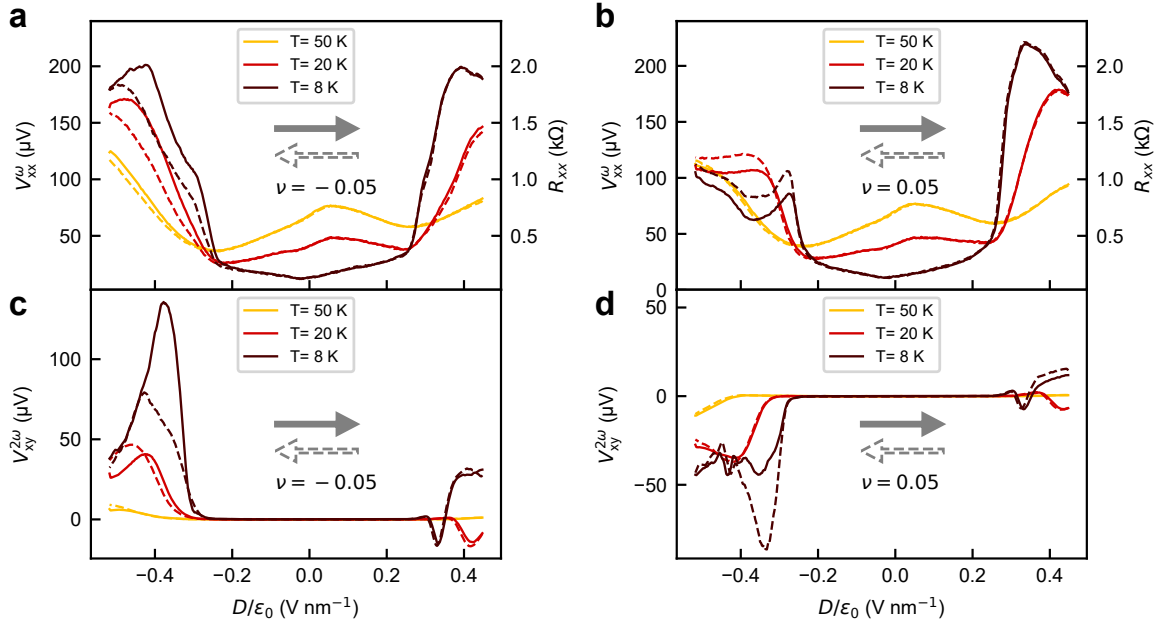
X Additional hysteresis data

X.1 Repeatability and histogram



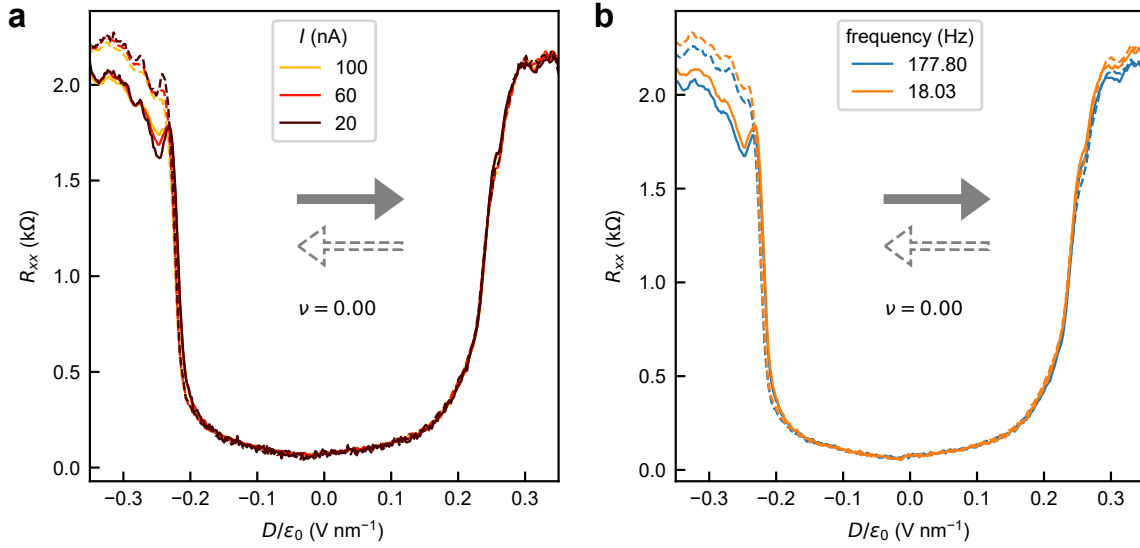
Supplementary Fig. S11. Switching statistics as a function of temperature. **a**, Variation of longitudinal voltage V_{xx}^{ω} with displacement field D/ϵ_0 (red colored plot corresponding to left axis, as indicated by the red arrow) when D/ϵ_0 is swept from left to right along the x-axis at a constant rate of $2.5 \text{ mV nm}^{-1} \text{ s}^{-1}$. The blue colored plot (corresponding to the right axis) shows the variation of the numerical derivative $\frac{dV_{xx}^{\omega}}{d(D/\epsilon_0)}$ with D/ϵ_0 . The data is plotted for the same direction of D/ϵ_0 for 59 cycles at a constant temperature of $T = 3.4$ K, indicating repeatability. **b**, The variation of V_{xx}^{ω} with D/ϵ_0 at few fixed temperatures. For each temperature, the data is plotted for 59 up cycles. **c-g**, Switching statistics at few fixed temperatures as mentioned in each subpanel. The histogram counts the position (in D/ϵ_0 axis) of the minima of $\frac{dV_{xx}^{\omega}}{d(D/\epsilon_0)}$ for the 59 up cycles at each fixed temperature.

X.2 Temperature dependence



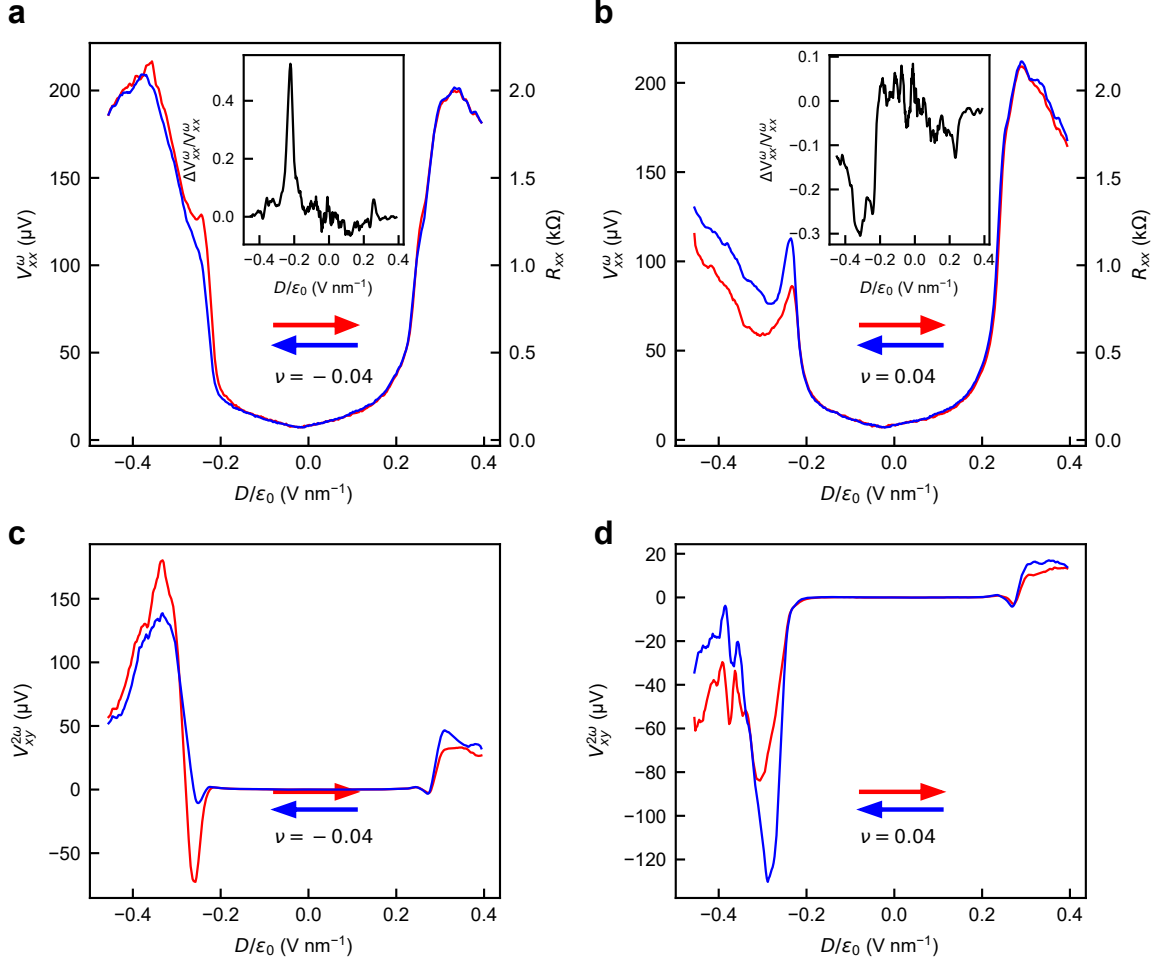
Supplementary Fig. S12. Temperature dependence of hysteresis in longitudinal and nonlinear Hall voltages. **a, b**, Variation of the longitudinal voltage, V_{xx}^{ω} with perpendicular displacement field (D/ϵ_0) for $\nu = -0.05$ (**a**) and $\nu = 0.05$ (**b**) at different fixed temperatures. The right axes indicate the corresponding longitudinal resistance, R_{xx} . **c, d**, Variation of the corresponding nonlinear Hall voltage, $V_{xy}^{2\omega}$ for $\nu = -0.05$ (**c**) and $\nu = 0.05$ (**d**) with D/ϵ_0 . The solid and dashed lines stand for the voltage response with increasing and decreasing values of D/ϵ_0 , respectively. The arrows indicate the sweep direction of D/ϵ_0 . The displacement field was swept at a constant rate of $2.5 \text{ mV nm}^{-1} \text{ s}^{-1}$.

X.3 Effect of current and frequency



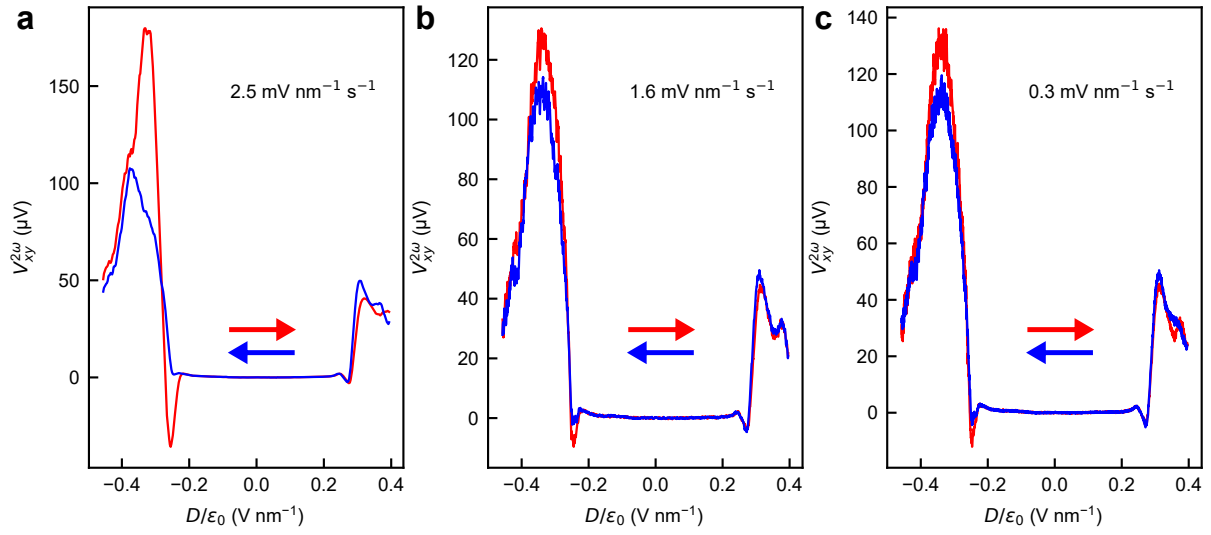
Supplementary Fig. S13. Current (I) (a) and frequency (b) dependence of hysteresis in longitudinal resistance R_{xx} with displacement field (D/ϵ_0) at a fixed temperature $T = 1.5$ K. The displacement field was swept at a constant rate of $2.5\text{ mV nm}^{-1}\text{ s}^{-1}$. Independence of hysteresis on value of driving current in **a** rules out any heating effect. Independence of hysteresis on frequency in **b** rules out any effect of stray capacitance.

X.4 Data for other fixed ν



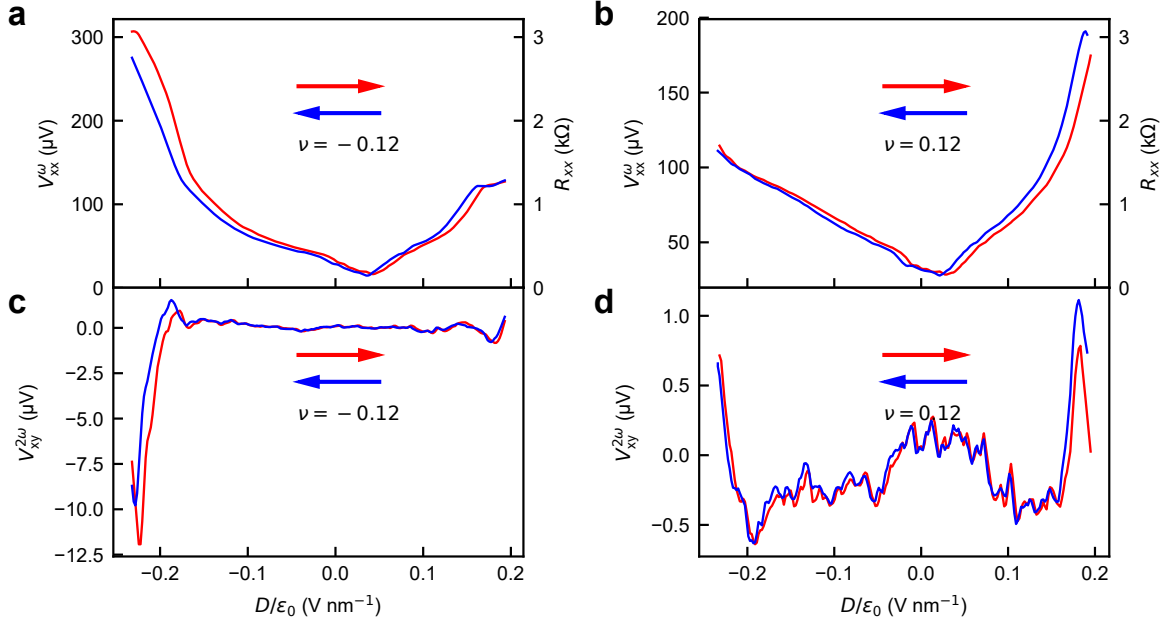
Supplementary Fig. S14. Dependence of sense of hysteresis on doping. **a, b**, Hysteresis in longitudinal resistance R_{xx} with displacement field (D/ϵ_0) for a doping below CNP at $\nu = -0.04$ (**a**) and above CNP at $\nu = 0.04$ (**b**). The arrows indicate direction of sweeping D . On the negative D side, the red curve leads the blue curve in **a**, while it lags in **b**. Such a change in hysteretic response due to doping cannot be accounted for via charge traps in dielectric. The insets show the relative difference in V_{xx}^ω of up and down sweep. The relative difference is maximum around $D/\epsilon_0 = -0.23 \text{ V nm}^{-1}$, where a topological transition takes place as discussed in main manuscript. Hysteresis in $V_{xy}^{2\omega}$ with displacement field (D/ϵ_0) for a doping below CNP at $\nu = -0.04$ (**c**) and above CNP at $\nu = 0.04$ (**d**), showing similar flipping in sense of hysteresis. The temperature was fixed at $T = 1.5 \text{ K}$ and the displacement field was swept at a constant rate of $2.5 \text{ mV nm}^{-1} \text{ s}^{-1}$.

X.5 Rate dependence



Supplementary Fig. S15. $V_{xy}^{2\omega}$ vs D/ϵ_0 hysteresis at a fixed $\nu = -0.05$ for three different rates of sweeping D/ϵ_0 at $2.5 \text{ mV nm}^{-1} \text{ s}^{-1}$ (a), $1.6 \text{ mV nm}^{-1} \text{ s}^{-1}$ (b), and $0.3 \text{ mV nm}^{-1} \text{ s}^{-1}$ (c).

X.6 hysteresis data from another device



Supplementary Fig. S16. Hysteresis in device-2 with twist angle of 1.26°. **a, b,** Variation of the longitudinal voltage V_{xx}^{ω} with perpendicular displacement field (D/ϵ_0) for a small negative filling (**a**) and positive filling (**b**) around CNP ($\nu = 0$). The right axes indicate the corresponding longitudinal resistance, R_{xx} . **c, d,** Variation of the nonlinear Hall voltage $V_{xy}^{2\omega}$ with D/ϵ_0 for similar small negative doping (**c**) and positive doping (**d**) around CNP. The red and blue solid lines stand for the voltage response with increasing and decreasing values of D/ϵ_0 , respectively. The arrows indicate the sweep direction of D/ϵ_0 . The displacement field was swept at a constant rate of 2.7 mV nm⁻¹ s⁻¹. The temperature was fixed at 10 mK. Measurement was performed with a current of 100 nA at a frequency of 177 Hz.

XI Polarization calculation details

XI.1 Computational Details

Our first-principles calculations are based on density functional theory (DFT) as implemented in Quantum ESPRESSO (QE) package [6]. We use ultrasoft pseudopotentials to represent the interaction between ionic cores and valence electrons. The exchange-correlation energy of electrons is treated within a generalized gradient approximation (GGA) [7] with a functional form parameterized by Perdew, Burke, and Ernzerhof [8]. We truncated the plane wave basis used in expansion of Kohn-Sham wave functions and charge density with energy cut-offs of 45 Ry and 360 Ry respectively. We used $18 \times 18 \times 1$ uniform grid of k-points for sampling the Brillouin zone (BZ) integrations. The discontinuity in occupation numbers of electronic states was smeared with broadening temperature of $k_B T = 0.005$ Ry using a Fermi-Dirac distribution function. We include van der Waals (vdW) interaction using PBE + D2 method of Grimme [9]. The 2D system is simulated using a periodic supercell, with a vacuum layer of 12 \AA separating adjacent periodic images of the sheet. To simulate response to electric field, we add a saw-tooth potential as a function z .

XI.2 Results and Discussion

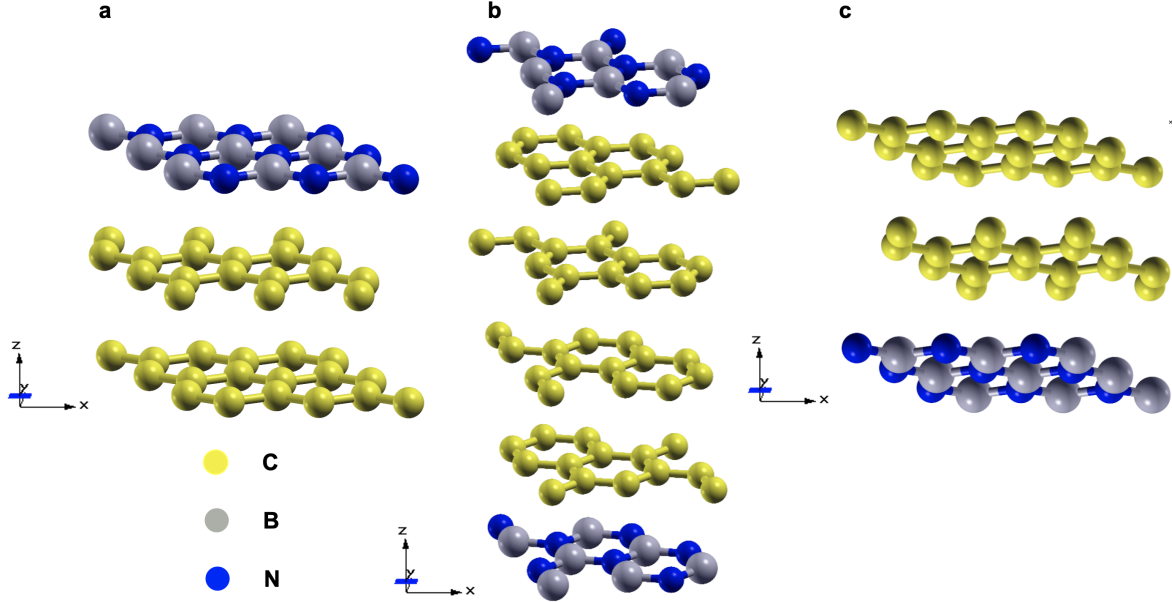
Twisted double bilayer graphene, TDBG, in our experiments is composed of two AB-stacked bilayers of graphene rotated by an angle [10] θ and encapsulated from top and bottom by hexagonal boron nitride (h-BN-TDBG-h-BN) (Supplementary Fig. S17b). Thus, parallelly stacked one atomic plane of hexagonal boron nitride and two layers of graphene (Gr-Gr-h-BN) is a building block making a half of h-BN-TDBG-h-BN (upper trilayer) (Supplementary Fig. S17a). Interestingly, a single Gr-Gr-h-BN unit is noncentrosymmetric and lacks the horizontal mirror symmetry. Hence, it is expected to have a non-vanishing polarization (dipole moment perpendicular to the plane). We consider two different configurations of Gr-Gr-h-BN which have been obtained by changing stacking sequences of Gr-Gr-h-BN (i) stacking of h-BN same as bottom graphene and (ii) stacking sequence of h-BN not matching with either of the two graphene layers. However, the energies of the two configurations are comparable (0.1 meV) and we carry out our theoretical analysis with the first configuration as a model.

We first examine the electronic structure of Gr-Gr-h-BN and find a band gap of ~ 26 meV at K point (h-BN breaks sublattice symmetry of AB-stacked bilayer graphene, Supplementary Fig. S18a). From the slope of macroscopic average electrostatic potential in vacuum, our estimate of polarization of Gr-Gr-h-BN is $P_z \approx -0.34 \mu\text{C}/\text{cm}^2$ (Extended Data Fig. 5b). Thus, Gr-Gr-h-BN has a nonzero polarization due to the broken inversion and horizontal reflection symmetries. This mechanism is similar to ferroelectricity in bilayer h-BN [4]. The lower trilayer of TDBG is h-BN-Gr-Gr (Supplementary Fig. S17c) and has exactly the same polarization with opposite sign.

The sense of hysteresis in longitudinal and nonlinear Hall voltage for doping just below charge neutrality point (CNP) is flipped on changing the doping to a point just above CNP. To understand the metastable states governing this hysteresis, we present a rigid band model for h-BN-Gr-Gr (lower trilayer) and Gr-Gr-h-BN (upper trilayer) of electronic states coupling with electric field and determine polarization as a function of electric field. Evolution of band energies with perpendicular electric field is modeled as

$$H_i = \epsilon_i + eE\langle Z_i \rangle \tag{S22}$$

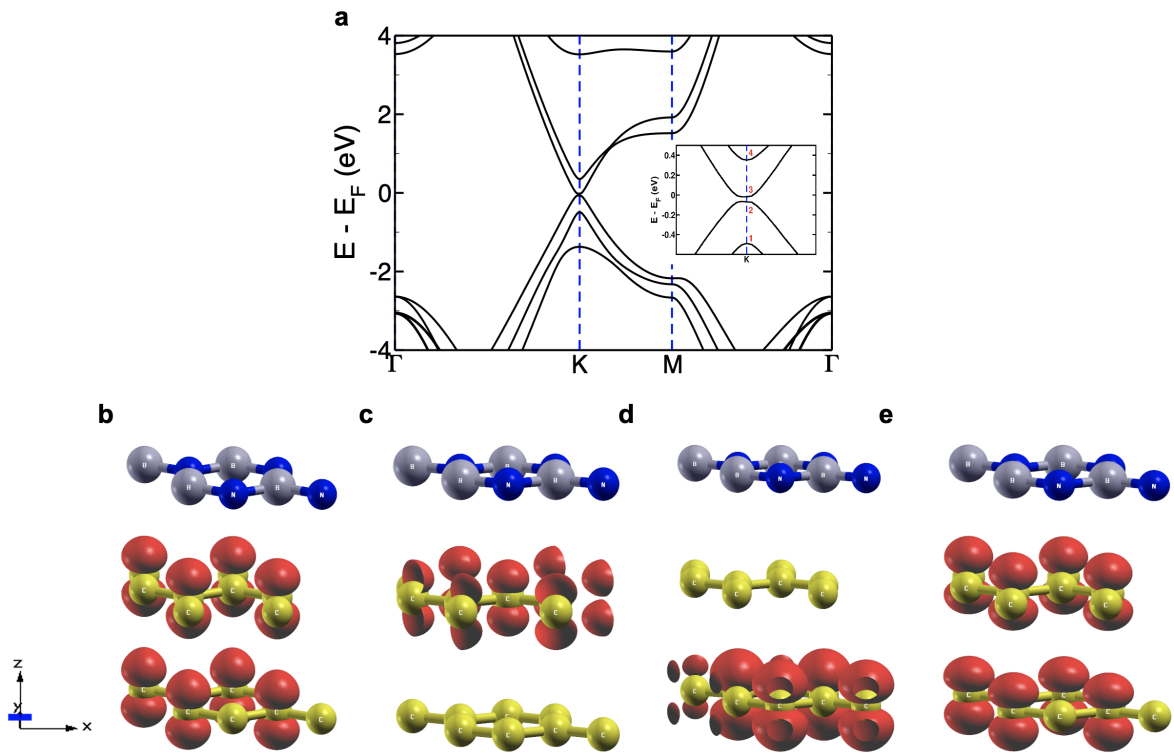
where i is the band index ($i = 1$ to 4 for the four bands close to Fermi at K point), ϵ_i is energy of i^{th} band, e is charge of an electron, E is electric field, $\langle Z \rangle$ is the average position of each state (Supplementary Fig. S18b-e). $\langle Z \rangle$ is minus (-) for h-BN-Gr-Gr (lower trilayer) and plus (+)



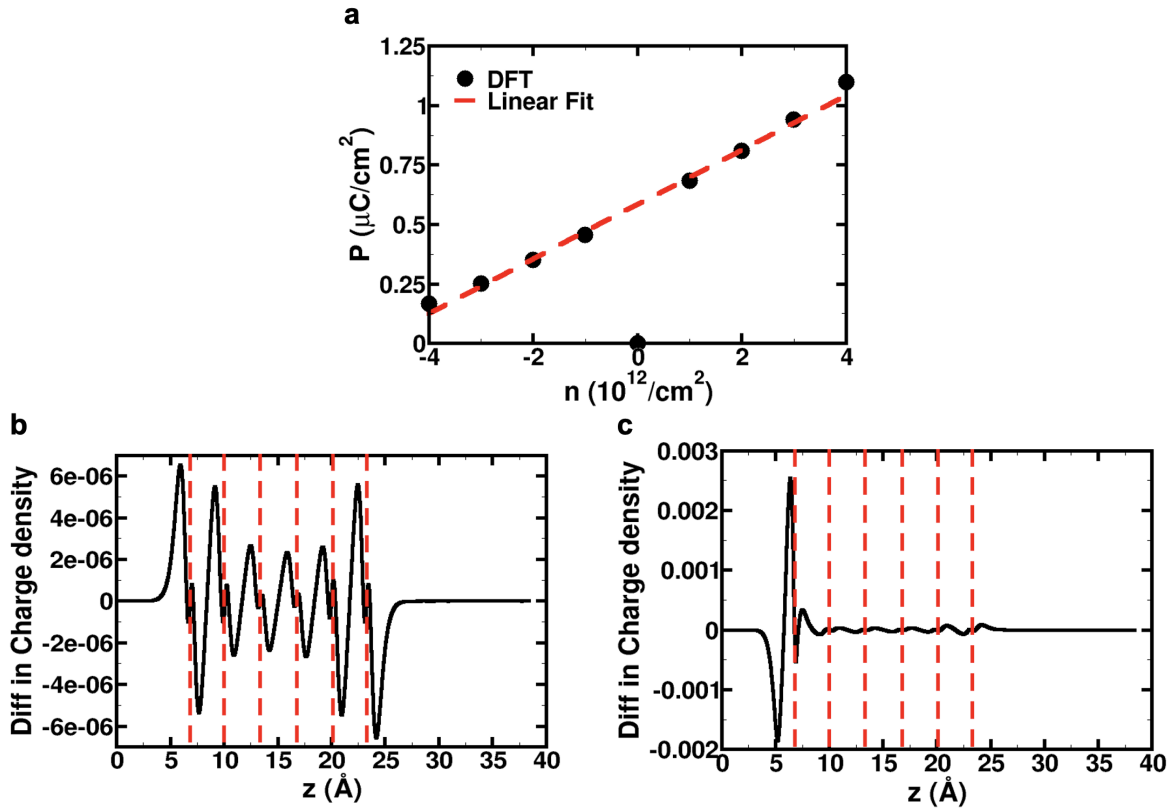
Supplementary Fig. S17. **a**, Structure of Gr-Gr-h-BN. **b**, Unit cell of twisted double bilayer graphene encapsulated between hexagonal boron nitride (h-BN-TDBG-h-BN) with a rotation angle of 21.78° . **c**, Structure of h-BN-Gr-Gr. The building blocks of h-BN-TDBG-h-BN are Gr-Gr-h-BN and h-BN-Gr-Gr. The atomic species C, B and N are displayed in yellow, grey and blue colors, respectively.

for Gr-Gr-h-BN (upper trilayer), respectively. Band 2 of the lower trilayer and band 3 of upper trilayer cross at $E = -0.0039 \text{ V/\AA}$ (band 3 of lower trilayer and band 2 of upper trilayer cross at $E = 0.0039 \text{ V/\AA}$), resulting in redistribution of charges among these bands (Extended Data Fig. 5c). We show that there exist two metastable states for (i) $E < -0.0039 \text{ V/\AA}$ and (ii) $E > 0.0039 \text{ V/\AA}$, with distinct polarization states in h-BN-TDBG-h-BN, that can be accessed with electric field within our rigid band model (Extended Data Fig. 5d). However, the resistance associated with the two metastable states remains the same. While the metastable states in h-BN-TDBG-h-BN are explained using the rigid band model, the hysteresis in resistance seen in experiments can originate from the broken symmetry, which can possibly arise from the distinction in coupling of top and bottom gates inducing inhomogeneous doping in the channel or by a twist between two trilayers.

To understand the role of a gate electrode, we obtain the difference in planar-averaged electron charge density, $\bar{\rho}(z)$ for $n = 4 \times 10^{12}/\text{cm}^2$, $E = 0.00625 \text{ V/\AA}$ and $n = 4 \times 10^{12}/\text{cm}^2$, $E = 0 \text{ V/\AA}$ with and without electric boundary conditions of a gate (Supplementary Fig. S19b and S19c) in h-BN-TDBG-h-BN with a twist angle $\theta = 21.78^\circ$. Asymmetry in $\Delta\bar{\rho}(z)$ at the atomic planes (red dashed lines in Supplementary Fig. S19b and S19c) indicate accumulation and depletion of electronic charge and local polarization arising from polarizability of p_z orbitals and a transfer of a tiny amount of charge. In the presence of gate, a positive electric field (along \hat{z}) pushes the electrons to the bottom gate (the scale of y-axis in Supplementary Fig. S19c is higher than Supplementary Fig. S19b), highlighting the inhomogeneity in doping. We note that a spontaneous electric dipole p_z can also arise from the restructuring of the regions with AA, AB, BA and BB stacking upon application of electric field [4] and contribute to the observed hysteresis.



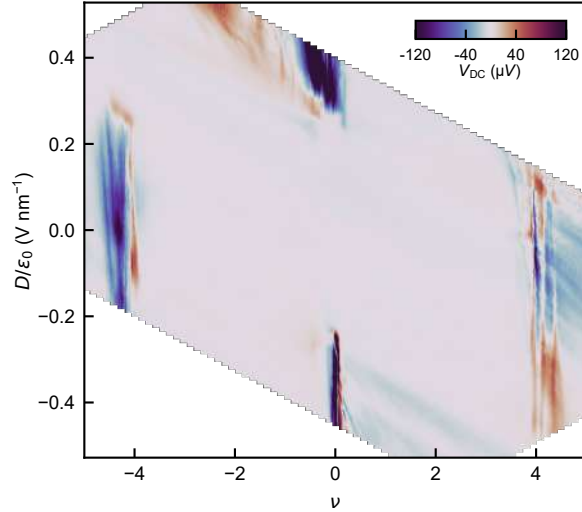
Supplementary Fig. S18. a, Electronic structure of Gr-Gr-h-BN shows a band gap of 26 meV at K point. **b-e**, Visualization of wavefunctions of four states near Fermi energy at K point of Band 1 (**b**), Band 2 (**c**), Band 3 (**d**) and Band 4 (**e**) of Gr-Gr-h-BN shows contribution from p_z orbitals of carbon of graphene. The average position, $\langle Z \rangle$ in terms of interlayer distance $d = 3.2 \text{ \AA}$ for bands 2 and 3 is $3/2d$, and $1/2d$, respectively.



Supplementary Fig. S19. **a**, Polarization in TDBG calculated as a function of doping in the presence of a bottom gate. **b**, **c**, The difference in planar-averaged electron charge density, $\bar{\rho}(z)$ for $n = 4 \times 10^{12}/\text{cm}^2$, $E = 0.00625 \text{ V/\AA}$ and $n = 4 \times 10^{12}/\text{cm}^2$, $E = 0 \text{ V/\AA}$ without (**b**) and with (**c**) gate set-up in h-BN-TDBG-h-BN with a twist angle $\theta = 21.78^\circ$. In the presence of gate, a positively oriented electric field pushes the electrons at the bottom gate (the scale of y-axis in **c** is higher than **b**).

XII DC voltage

Apart from the second harmonic voltage $V_{xy}^{2\omega}$, the nonlinear Hall effect also gives rise to a DC voltage [11, 17]. In Supplementary Fig. S20, we show the measured DC voltage in perpendicular direction to an ac current applied with frequency 177 Hz. The dependence of the DC voltage is shown for the full parameter space of (ν, D) for the same device used to show the NLH voltage dependence in Fig. 2b of main manuscript. DC voltage, together with the measured second harmonic $V_{xy}^{2\omega}$, provides additional evidence for NLH effect in TDBG devices.



Supplementary Fig. S20. Dependence of DC voltage on filling factor and displacement field. DC voltage (V_{DC}) as a function of filling factor (ν) and displacement field (D/ϵ_0) measured perpendicular to current $I = 100$ nA applied with a frequency of 177 Hz. The color bar provided in top right indicates the corresponding values of V_{DC} .

References

- [1] Bistritzer, R. & MacDonald, A. H. Moiré bands in twisted double-layer graphene. *Proceedings of the National Academy of Sciences* **108**, 12233–12237 (2011).
- [2] Bi, Z., Yuan, N. F. Q. & Fu, L. Designing flat bands by strain. *Physical Review B* **100**, 035448 (2019).
- [3] Wang, Y.-X., Li, F. & Zhang, Z.-Y. Phase diagram and orbital chern insulator in twisted double bilayer graphene. *Physical Review B* **103**, 115201 (2021).
- [4] Koshino, M. Band structure and topological properties of twisted double bilayer graphene. *Physical Review B* **99**, 235406 (2019).
- [5] Mohan, P., Ghorai, U. & Sensarma, R. Trigonal warping, satellite dirac points, and multiple field tuned topological transitions in twisted double bilayer graphene. *Physical Review B* **103**, 155149 (2021).
- [6] Giannozzi, P. *et al.* Quantum espresso: a modular and open-source software project for quantum simulations of materials. *Journal of physics: Condensed matter* **21**, 395502 (2009).
- [7] Hua, X., Chen, X. & Goddard, W. Generalized generalized gradient approximation: An improved density-functional theory for accurate orbital eigenvalues. *Physical Review B* **55**, 16103 (1997).
- [8] Perdew, J., Burke, K. & Ernzerhof, M. Perdew, Burke, and Ernzerhof reply. *Physical Review Letters* **80**, 891 (1998).
- [9] Grimme, S. Accurate description of van der Waals complexes by density functional theory including empirical corrections. *Journal of computational chemistry* **25**, 1463–1473 (2004).

- [10] Cocemasov, A. I., Nika, D. L. & Balandin, A. A. Phonons in twisted bilayer graphene. *Physical Review B* **88**, 035428 (2013).